

Timing and climate forcing of volcanic eruptions for the past 2,500 years

M. Sigl¹†, M. Winstrup², J. R. McConnell¹, K. C. Welten³, G. Plunkett⁴, F. Ludlow⁵, U. Büntgen^{6,7,8}, M. Caffee^{9,10}, N. Chellman¹, D. Dahl-Jensen¹¹, H. Fischer^{7,12}, S. Kipfstuhl¹³, C. Kostick¹⁴, O. J. Maselli¹, F. Mekhaldi¹⁵, R. Mulvaney¹⁶, R. Muscheler¹⁵, D. R. Pasteris¹, J. R. Pilcher⁴, M. Salzer¹⁷, S. Schüpbach^{7,12}, J. P. Steffensen¹¹, B. M. Vinther¹¹ & T. E. Woodruff⁹

Volcanic eruptions contribute to climate variability, but quantifying these contributions has been limited by inconsistencies in the timing of atmospheric volcanic aerosol loading determined from ice cores and subsequent cooling from climate proxies such as tree rings. Here we resolve these inconsistencies and show that large eruptions in the tropics and high latitudes were primary drivers of interannual-to-decadal temperature variability in the Northern Hemisphere during the past 2,500 years. Our results are based on new records of atmospheric aerosol loading developed from high-resolution, multi-parameter measurements from an array of Greenland and Antarctic ice cores as well as distinctive age markers to constrain chronologies. Overall, cooling was proportional to the magnitude of volcanic forcing and persisted for up to ten years after some of the largest eruptive episodes. Our revised timescale more firmly implicates volcanic eruptions as catalysts in the major sixth-century pandemics, famines, and socioeconomic disruptions in Eurasia and Mesoamerica while allowing multi-millennium quantification of climate response to volcanic forcing.

Volcanic eruptions are primary drivers of natural climate variability—their sulfate aerosol injections into the stratosphere shield the Earth's surface from incoming solar radiation, leading to short-term cooling at regional-to-global scales¹. Temperatures during the past 2,000 years have been reconstructed at regional², continental³, and global scales⁴ using proxy information from natural archives. Tree-ring-based proxies provide the vast majority of climate records from mid- to high-latitude regions of (predominantly) the Northern Hemisphere, whereas ice-core records (for example, $\delta^{18}\text{O}$) represent both polar regions³.

Climate forcing reconstructions for the Common Era (CE)—including solar (for example, ¹⁰Be)⁵ and volcanic (for example, sulfate)^{6,7} activity—derive mostly from ice-core proxies. Any attempt to attribute reconstructed climate variability to external volcanic forcing, and to distinguish between response, feedback, and internal variability of the climate system, requires ice-core chronologies that are synchronous with those of other climate reconstructions. In addition, multi-proxy climate reconstructions^{2–4} derived from ice cores and other proxies such as tree rings will have diminished high- to mid-frequency amplitudes if the individual climate records are on different timescales.

The magnitudes and relative timing of simulated Northern Hemisphere temperature responses to large volcanic eruptions are in disagreement with reconstructed temperatures obtained from tree rings^{8,9}, but it is unclear to what extent this model/data mismatch is caused by limitations in temperature reconstructions, volcanic reconstructions, or implementation of aerosol forcing in climate models^{9–11}. The hypothesis of chronological errors in tree-ring-based

temperature reconstructions^{8,9} offered to explain this model/data mismatch has been tested and widely rejected^{11–14}, while new ice-core records have become available providing different eruption ages^{15,16} and more precise estimates of atmospheric aerosol mass loading¹⁷ than for previous volcanic reconstructions.

Using documented¹⁸ and previous ice-core-based eruption ages¹⁶, strong summer cooling following large volcanic eruptions has been recorded in tree-ring-based temperature reconstructions during the second millennium CE with a one-to-two year lag similar to that observed in instrumental records after the 1991 Pinatubo eruption¹⁹. An apparent seven-year delayed cooling observed in individual tree-ring series relative to Greenland ice-core acidity peaks during the first millennium CE, however, suggests a bias in existing ice-core chronologies^{20,21}. Using published ice-core chronologies, we also observed a seven-year offset between sulfate deposition in North Greenland and the start of tree-ring growth reduction in a composite of five multi-centennial tree-ring summer temperature reconstructions ('N-Tree') from the Northern Hemisphere between 1 and 1000 CE (Methods), whereas tree-ring response was effectively immediate for eruptions occurring after 1250 CE (Fig. 1a).

Precise time marker across hemispheres

Independent age markers with which to test the accuracy of tree-ring and ice-core chronologies have recently become available with the detection of abrupt enrichment events in the ¹⁴C content of tree rings. Rapid increases of atmospheric ¹⁴C were first identified in individual growth increments of cedars from Japan between 774 CE and 775 CE²² and between 993 CE and 994 CE²³. The presence and timing of

¹Desert Research Institute, Nevada System of Higher Education, Reno, Nevada 89512, USA. ²Department of Earth and Space Sciences, University of Washington, Seattle, Washington 98195, USA. ³Space Sciences Laboratory, University of California, Berkeley, California 94720, USA. ⁴School of Geography, Archaeology and Palaeoecology, Queen's University Belfast, Belfast BT7 1NN, UK. ⁵Yale Climate and Energy Institute, and Department of History, Yale University, New Haven, Connecticut 06511, USA. ⁶Swiss Federal Research Institute WSL, 8903 Birmensdorf, Switzerland. ⁷Oeschger Centre for Climate Change Research, University of Bern, 3012 Bern, Switzerland. ⁸Global Change Research Centre AS CR, 60300 Brno, Czech Republic. ⁹Department of Physics, Purdue University, West Lafayette, Indiana 47907, USA. ¹⁰Department of Earth, Atmospheric, and Planetary Sciences, Purdue University, West Lafayette, Indiana 47907, USA. ¹¹Centre for Ice and Climate, Niels Bohr Institute, University of Copenhagen, 2100 Copenhagen, Denmark. ¹²Climate and Environmental Physics, University of Bern, 3012 Bern, Switzerland. ¹³Alfred-Wegener-Institut Helmholtz-Zentrum für Polar- und Meeresforschung, 27570 Bremerhaven, Germany. ¹⁴Department of History, The University of Nottingham, Nottingham NG7 2RD, UK. ¹⁵Department of Geology, Quaternary Sciences, Lund University, 22362 Lund, Sweden. ¹⁶British Antarctic Survey, Natural Environment Research Council, Cambridge CB3 0ET, UK. ¹⁷The Laboratory of Tree-Ring Research, University of Arizona, Tucson, Arizona 85721, USA. †Present address: Laboratory of Radiochemistry and Environmental Chemistry, Paul Scherrer Institut, 5232 Villigen, Switzerland.

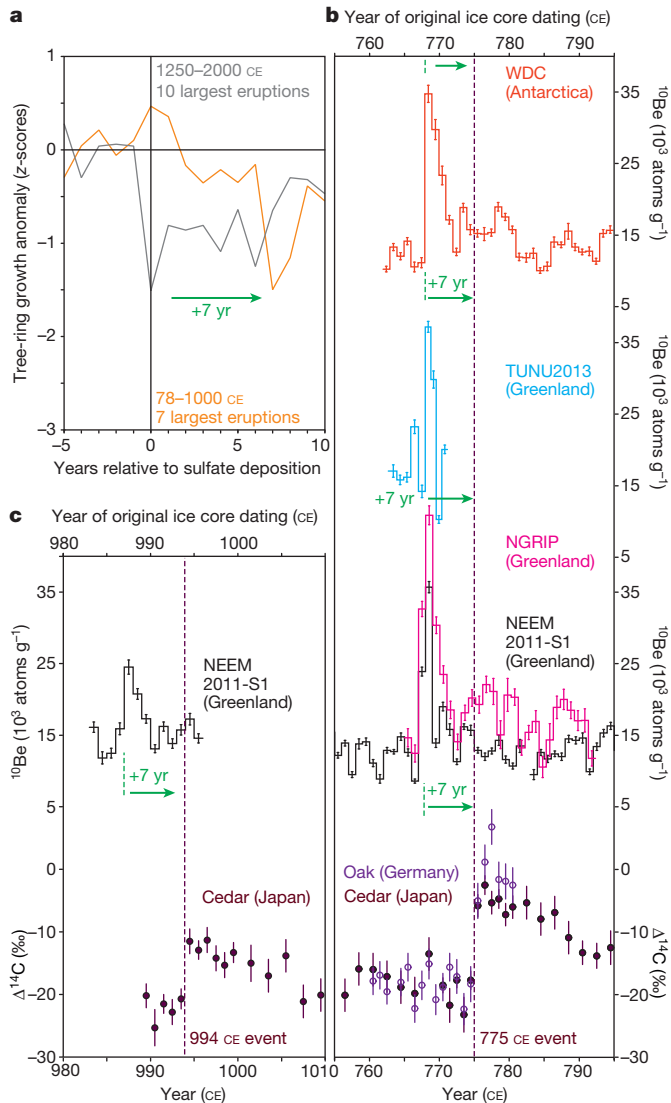


Figure 1 | Annual ^{10}Be ice-core records and post-volcanic cooling from tree rings under existing ice-core chronologies. **a**, Superposed epoch analysis for the largest volcanic signals in NEEM-2011-S1 between 78 and 1000 CE ($n = 7$; orange trace) and for the largest eruptions between 1250 and 2000 CE ($n = 10$; grey trace)¹⁶. Shown are standardized growth anomalies (z scores relative to 1000–1099 CE) from a multi-centennial, temperature-sensitive tree-ring composite (N-Tree^{42,43,76–78}, Methods) ten years after the year of volcanic sulfate deposition at the NEEM ice core site in Greenland (GICC05 timescale), relative to the level five years before sulfate deposition. **b**, Annually resolved ^{10}Be concentration records from the WDC, TUNU2013, NGRIP, and NEEM-2011-S1 ice cores on their original timescales and annually resolved $\Delta^{14}\text{C}$ series from tree-ring records between 755 CE and 795 CE^{22,24}, with green arrows representing the suggested time shifts for synchronization; error bars are 1σ measurement uncertainties; the estimated relative age uncertainty for TUNU2013 at this depth interval from volcanic synchronization with NEEM-2011-S1 is ± 1 year. **c**, Annually resolved ^{10}Be concentration record from NEEM-2011-S1 ice core on its original timescale and annually resolved $\Delta^{14}\text{C}$ series from tree rings in 980 CE and 1010 CE²³; error bars are 1σ measurement uncertainties.

the event in 775 CE (henceforth, the 775 event) has been reproduced by all radiocarbon measurements performed on tree rings at annual (or higher) resolution—including tree cores from Germany²⁴, the Alps¹², the Great Basin²⁵ (USA), and Siberia²⁵. Recent identification of the same 775 CE event in kauri wood samples from New Zealand in the Southern Hemisphere demonstrates the global extent of the rapid ^{14}C increase and provides further constraints on the event's exact timing (March 775 ± 6 months) owing to the asynchronous

Southern Hemisphere growing season²⁶. While the cause of the 775 and 994 events is still debated^{22,24,27}, we expect that they might also have produced an excess of cosmogenic ^{10}Be through the interaction of high-energy particles with atmospheric constituents^{28,29}. Since both of these radionuclides are incorporated rapidly into proxy archives via aerosol deposition (^{10}Be in ice cores) and photosynthesis ($^{14}\text{CO}_2$ in tree rings), isotopic anomalies caused by these extraterrestrial events provide a global age marker with which to link ice-core records to tree-ring chronologies directly²⁷. The latter serve as an absolute and precise age marker, verified (at least since 775 CE) by the coherence of the rapid increase in ^{14}C in all tree-ring records for which high-resolution radiocarbon analyses were performed, including those speculated to be at risk of missing rings⁸.

We measured ^{10}Be concentrations at approximately annual resolution in four ice cores—NEEM-2011-S1, TUNU2013, and NGRIP in Greenland, and the West Antarctic Ice Sheet Divide Core (WDC)—over depth ranges encompassing the year 775 CE as dated in existing ice-core chronologies in order to provide a direct, physically based test of any dating bias in these chronologies (Fig. 1, Extended Data Fig. 1, Methods, Supplementary Data 1). Both polar ice sheets contain ^{10}Be concentrations exceeding the natural background concentration ($>150\%$; 6σ) for one-to-two consecutive years, compatible with the 775 CE event observed in tree rings. Using the original ice-core age models^{16,30}, the ages of the ^{10}Be maxima in NEEM-2011-S1, NGRIP, and WDC are 768 CE, offset by 7 years from the tree-ring event. A further ^{10}Be anomaly measured in NEEM-2011-S1 at 987 CE, compatible with the 994 CE event in tree rings, suggests that a chronological offset was present by the end of the first millennium CE (Fig. 1). Several different causes may have contributed to the offset (see a summary in the Methods section), among which is the use of a previous dating constraint³⁰ for Greenland, where volcanic fallout in the ice was believed to indicate the historic (79 CE) eruption of Vesuvius.

Revised ice-core chronologies

Given the detection of a bias in existing ice-core chronologies, we developed new timescales before the 1257 Samalas eruption in Indonesia³¹ using highly resolved, multi-parameter aerosol concentration records from three ice cores: NEEM-2011-S1, NEEM, and WDC. We used the StratiCounter program, an automated, objective, annual-layer detection method based on Hidden Markov Model (HMM) algorithms³² (Methods). For NEEM-2011-S1, the confidence intervals obtained for the layer counts allowed us to improve the dating further by constraining the timescale using the 775 CE ^{10}Be anomaly and three precisely dated observations of post-volcanic aerosol loading of the atmosphere (Fig. 2, Extended Data Tables 1–3, Methods, Supplementary Data S2).

We evaluated the accuracy of our new chronologies ('WD2014' for WDC and 'NS1-2011' for NEEM) by comparison to (1) an extensive database of historical volcanic dust veil observations (Extended Data Fig. 2, Methods, Supplementary Data 2), (2) ice-core tephra evidence (Methods), and (3) the 994 CE event (Methods, Fig. 2). Using the new timescales, we found large sulfate signals in Greenland (for example, in 682 CE, 574 CE, and 540 CE) between 500 CE and 2000 CE that frequently occurred within one year of comparable—and independently dated—signals in Antarctica. These bipolar signals can now be confidently attributed to large tropical eruptions (Fig. 2). Back to 400 BCE, other large sulfate peaks (for example, 44 BCE) were synchronous to within three years (Fig. 2). We conclude that the revised ice-core timescales are accurate to within less than five years during the past 2,500 years, on the basis of combined evidence from radionuclides, tree rings, tephra analyses, and historical accounts. Compared to the previous chronologies, age models differ before 1250 CE by up to 11 years (GICC05, Greenland) and 14 years (WDC06A-7, Antarctica) (Extended Data Fig. 3).

Figure 2 | Re-dated ice-core, non-sea-salt sulfur records from Greenland and Antarctica in relation to growth anomalies in the N-Tree composite.

a, Ice-core, non-sea-salt sulfur (nssS in parts per billion, p.p.b.) records from Greenland (NEEM, NEEM-2011-S1) on the NS1-2011 timescale between 500 BCE and 1300 CE, with the identified layer of Tianchi tephra⁶⁷ highlighted (orange star). Calendar years are given for the start of volcanic sulfate deposition. Events used as fixed age markers to constrain the dating (536 CE, 626 CE, 775 CE, 939 CE and 1258 CE) are indicated (purple stars). Annually resolved ¹⁰Be concentration record (green) from NEEM-2011-S1 encompassing the two $\Delta^{14}\text{C}$ excursion events in trees from 775 CE and 994 CE. **b**, Tree-ring growth anomalies (relative to 1000–1099 CE) for the N-Tree composite^{42,43,76–78}. **c**, nssS records from Antarctica (red, WDC; pink, B40) on the WD2014 timescale and annually resolved ¹⁰Be concentrations from WDC. **d**, Superposed epoch analysis for 28 large volcanic signals during the past 2,500 years. Tree-ring growth anomalies relative to the timing of reconstructed sulfate deposition in Greenland (NS1-2011) are shown for 1250–2000 CE (black trace) and 500 BCE to 1250 CE (green trace).

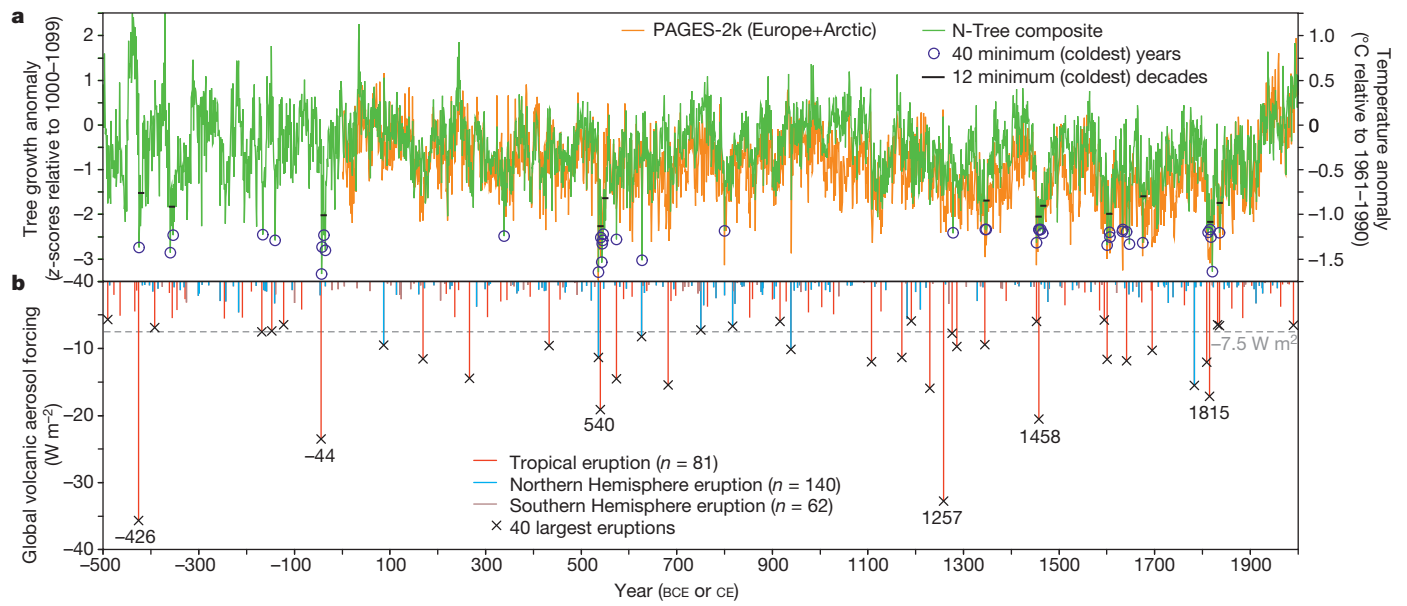
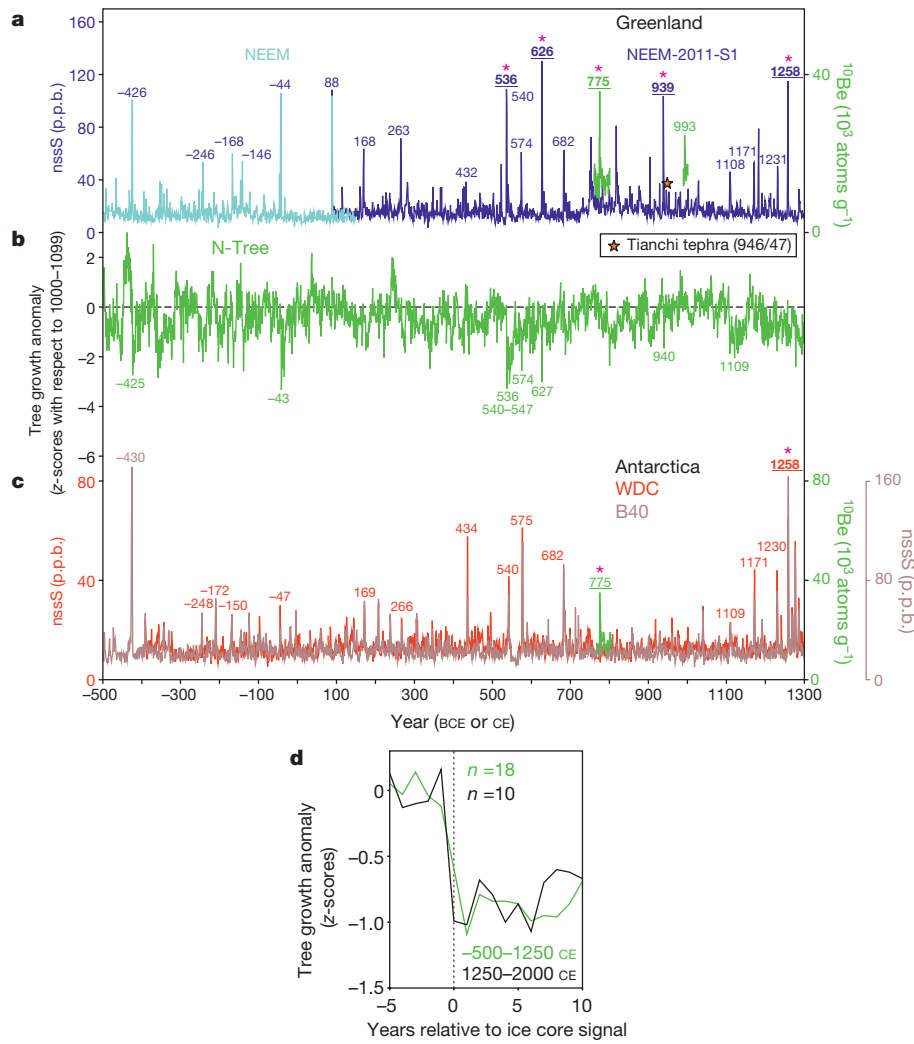


Figure 3 | Global volcanic aerosol forcing and Northern Hemisphere temperature variations for the past 2,500 years. **a**, 2,500-year record of tree-growth anomalies (N-Tree^{42,43,76–78}; relative to 1000–1099 CE) and reconstructed summer temperature anomalies for Europe and the Arctic³ with the 40 coldest single years and the 12 coldest decades based on N-Tree indicated. **b**, Reconstructed global volcanic aerosol forcing from bipolar sulfate composite

records from tropical (bipolar), Northern Hemisphere, and Southern Hemisphere eruptions. Total (that is, time-integrated) forcing values are calculated by summing the annual values for the duration of volcanic sulfur deposition. The 40 largest volcanic signals are indicated, and ages are given for events representing atmospheric sulfate loading exceeding that of the Tambora 1815 eruption.

History of volcanic forcing

Employing our revised timescales and new high-resolution, ice-core sulfur measurements, we developed an extended reconstruction of volcanic aerosol deposition since early Roman times for both polar ice sheets, from which we then estimated radiative forcing using established transfer functions¹⁵ (Fig. 3, Methods, Supplementary Data 3–5). This forcing series is characterized by improved dating accuracy, annual resolution, and a larger number of ice-core records in the Antarctic ice-core sulfate composite¹⁷ than in previous reconstructions^{6,7}. It spans 2,500 years, allowing investigation of climate–volcano linkages more accurately and earlier than with previous reconstructions. It also provides a perspective on volcanic influences during major historical epochs, such as the growth of Roman imperial power and subsequent decline during the ‘Migration Period’ (the early part of the first millennium CE) in Europe—times of (1) demographic and economic expansion as well as relative societal stability and (2) political turmoil and population instability, respectively³³. With improved dating and lower volcanic-sulfate detection limits from the Antarctic array¹⁷, we were able to detect, estimate, and attribute volcanic aerosol loading and forcing from 283 individual eruptive events during this period (Fig. 3).

We attributed about half of these to mid- to high-latitude Northern Hemisphere sources, while 81 were attributed to tropical eruptions (having synchronous sulfate deposition on both polar ice sheets).

These tropical volcanic eruptions contributed 64% of total volcanic forcing throughout the period, with five events exceeding the sulfate loading from the 1815 Tambora eruption in Indonesia (Fig. 3, Extended Data Table 4). Events in 426 BCE and 44 BCE rival the great 1257 CE Samalas eruption as the largest sulfate-producing eruptions during this time. These two earlier events have not been widely regarded as large tropical eruptions with potential for strong climate impact²⁰, owing to the lack of complete and synchronized sulfate records from Greenland and Antarctica. We base the claim that these two eruptions were tropical in origin and caused large radiative perturbations on the observation that ice cores from Greenland and Antarctica record coeval (within their respective age uncertainties) and exceptionally high volcanic sulfate concentrations. Both of these events were followed by strong and persistent growth reduction in tree-ring records³⁴ (Fig. 2) as is typically observed after large tropical eruptions during the Common Era (Fig. 3).

Post-volcanic summer cooling

Superposed epoch analyses (Methods) performed on the ‘N-Tree’ composite record centred on the largest volcanic signals between 500 BCE and 1250 CE as well as between 1250 CE and 2000 CE, show a clear post-volcanic cooling signal. For both periods, maximum tree-ring response lagged the date of initial increase of sulfate deposition by one year (Fig. 2), consistent with the response observed if using only

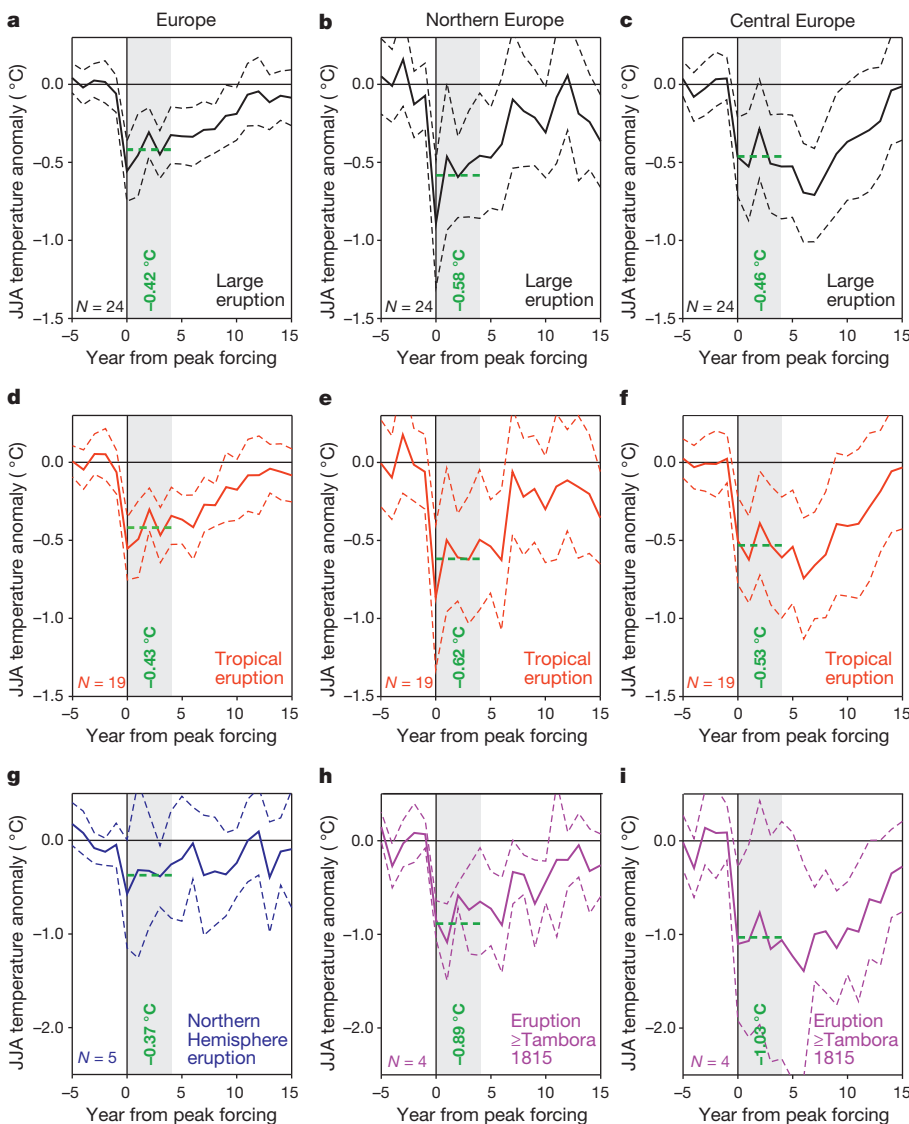


Figure 4 | Post-volcanic cooling. Superposed composites (time segments from selected periods in the Common Era positioned so that the years with peak negative forcing are aligned) of the JJA (June, July and August) temperature response to the 24 largest eruptions (exceeding the Pinatubo 1991 eruption). **a–c**, For three regional reconstructions in Europe^{3,35,42}. **d–f**, For the 19 largest tropical eruptions. **g**, For the five largest Northern Hemisphere eruptions. **h, i**, For the eruptions with negative forcing larger than that of the Tambora 1815 eruption for Northern Europe (**h**) and for Central Europe (**i**). Note the different scale for **g–i**. JJA temperature anomalies (in °C) for 15 years after reconstructed volcanic peak forcing, relative to the five years before the volcanic eruption, are shown. Dashed lines present twice the standard error of the mean (2 s.e.m.) of the temperature anomalies associated with the multiple eruptions. Five-year average post-volcanic temperatures are shown for each reconstruction (lag 0 to lag +4 years, grey shading).

historically documented eruptions with secure dating for the past 800 years¹⁸. The sharp and immediate (that is, less than one year lag time) response of tree growth to the ice-core volcanic signal throughout the past 2,500 years further corroborates the accuracy of our new ice-core timescales (Extended Data Fig. 4).

Of the 16 most negative tree-growth anomalies (that is, the coldest summers) between 500 BCE and 1000 CE, 15 followed large volcanic signals—with the four coldest (43 BCE, 536 CE, 543 CE, and 627 CE) occurring shortly after several of the largest events (Extended Data Tables 4 and 5). Similarly, the coldest summers in Europe during the Common Era³ were associated with large volcanic eruptions (Extended Data Table 5). Reduced tree growth after volcanic eruptions was also prominent in decadal averages of the ‘N-Tree’ composite. All 16 decades with the most reduced tree growth for our 2,500-year period followed large eruptions (Fig. 3, Extended Data Table 5). In many cases, such as the coldest decade, from 536 CE to 545 CE³, sustained cooling was associated with the combined effect of several successive volcanic eruptions.

Strong post-volcanic cooling was not restricted to tropical eruptions; it also followed Northern Hemisphere eruptions (Fig. 4), with maximum cooling in the year of volcanic-sulfate deposition. In contrast to the average of the 19 largest CE tropical eruptions, however, the Northern-Hemisphere-only eruptions did not give rise to any noticeable long-term cooling effect (Fig. 4). The persistence of implied post-volcanic cooling following the largest tropical eruptions is strongly expressed in temperature reconstructions based on tree-ring width measurements (for example, those from the Alps), with recovery times of more than ten years. Persistent cooling, with temperature reduction notably below the pre-eruption baseline for six consecutive years, is also observed in temperature reconstructions based on maximum latewood density (for example, those from Northern Scandinavia), which is the preferred proxy with which to quantify volcanic cooling contributions on climate owing to its less marked biological memory effects³⁵ (Fig. 4). These findings indicate that eruption-induced climate anomalies following large tropical eruptions may last longer than is indicated in many climate simulations (<3–5 years)^{9,36,37} and that potential positive feedbacks initiated after

large tropical eruptions (for example, sea-ice feedbacks) may not be adequately represented in climate simulations^{38,39}.

The five-year averaged (lag 0 to lag 4 years) cooling response over three Northern Hemisphere regions (Methods) following the 19 largest Common Era tropical eruptions was -0.6 ± 0.2 °C (two standard errors of the mean, 2 s.e.m.), and that of large Northern Hemisphere eruptions was -0.4 ± 0.4 °C, with the strongest cooling induced in the high latitudes. Overall, cooling was proportional to the magnitude of volcanic forcing, with stratospheric sulfate loading exceeding that of the Tambora eruption inducing the strongest response of -1.1 ± 0.6 °C (Figs 3 and 4).

Global climate anomalies in 536–550 CE

Our new dating allowed us to clarify long-standing debates concerning the origin and consequences of the severe and apparently global climate anomalies observed in the period 536–550 CE, which began with the recognition of the “mystery cloud” of 536 CE⁴⁰ observed in the Mediterranean basin. Under previous ice-core dating, it has been argued that this dust veil corresponded to an unknown tropical eruption dated 533–534 CE (± 2 years)⁴¹. Using our revised timescales, we found at least two large volcanic eruptions around this period (Fig. 5).

The first eruptive episode in 535 CE or early 536 CE injected large amounts of sulfate and ash into the atmosphere, apparently in the Northern Hemisphere. Geochemistry of tephra filtered from the NEEM-2011-S1 ice core at a depth corresponding to 536 CE indicated multiple North American volcanoes as likely candidates for a combined volcanic signal (Extended Data Fig. 5, Methods, Supplementary Data 5). Historical observations (Extended Data Table 3) identified atmospheric dimming as early as 24 March 536 CE, and lasting up to 18 months. The summer of 536 CE appeared exceptionally cold in all tree-ring reconstructions in the extra-tropical Northern Hemisphere from North America³⁴, over Europe^{35,42,43} to Asia⁴⁴. Depending on the reconstruction method used, European summer temperatures in 536 CE dropped 1.6–2.5 °C relative to the previous 30-year average³.

The second eruptive episode in 539 CE or 540 CE, identified in both Greenland and Antarctica ice-core records and hence probably tropical in origin, resulted in up to 10% higher global aerosol loading than

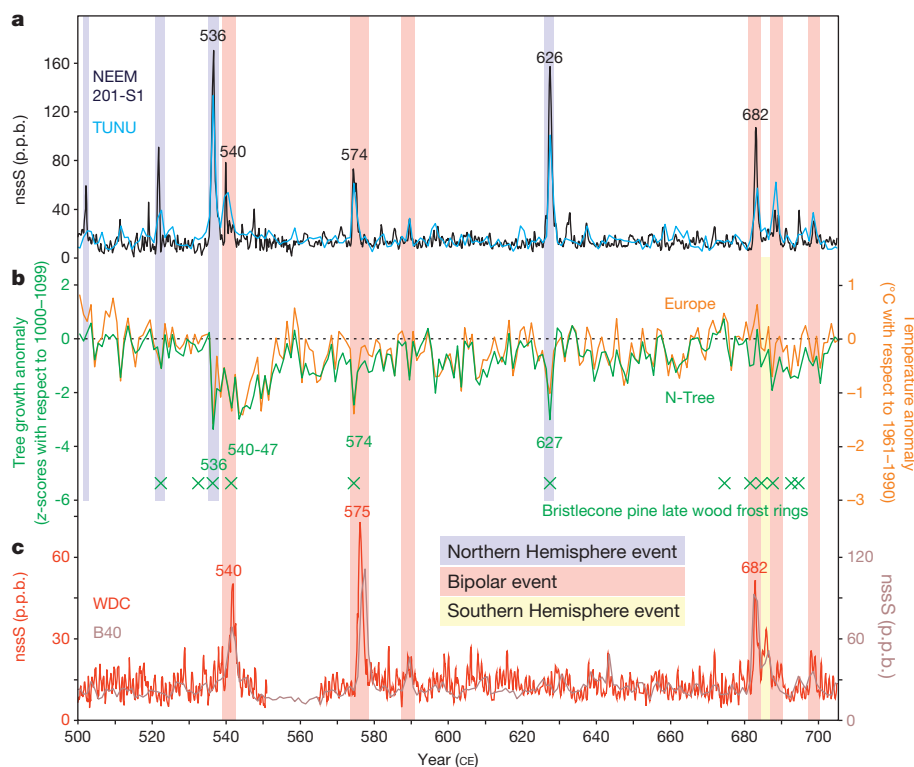


Figure 5 | Volcanism and temperature variability during the migration period (500–705 CE). **a**, Ice-core non-sea-salt sulphur (nssS) records from Greenland (black trace, NEEM-2011-S1; blue trace, TUNU2013). Calendar years for five large eruptions are given for the start of volcanic sulfate deposition. **b**, Summer temperature anomalies (orange trace) for Europe³, and reconstructed N-Tree growth anomalies (green trace) and occurrence of frost rings in North American bristlecone pine tree-ring records. **c**, nssS records from Antarctica (red trace, WDC; pink trace, B40) on the WD2014 timescale; attribution of the sulfur signals to bipolar, Northern Hemisphere, and Southern Hemisphere events based on the timing of deposition on the two independent timescales is indicated by shading.

the Tambora 1815 eruption reconstructed from our bipolar sulfate records. Summer temperatures consequently dropped again, by 1.4–2.7 °C in Europe in 541 CE³, and cold temperatures persisted in the Northern Hemisphere until almost 550 CE^{3,33,34,42} (Figs 2, 3, 5).

This provides a notable environmental context to widespread famine and the great Justinian Plague of 541–543 CE that was responsible for decimating populations in the Mediterranean and potentially China^{45,46}. Although certain climatic conditions (for example, wet summers) have been linked to plague outbreaks in the past⁴⁷, a direct causal connection of these two large volcanic episodes and subsequent cooling to crop failures and outbreaks of famines and plagues is difficult to prove³³. However, the exact delineation of two of the largest volcanic signals—with exceptionally strong and prolonged Northern Hemisphere cooling, written evidence of famines and pandemics, as well as the socio-economic decline observed in Mesoamerica (the “Maya Hiatus”⁴⁸), Europe, and Asia—supports the idea that the latter may be causally associated with volcanically induced climatic extremes.

Detailed study of major volcanic events during the sixth century (Fig. 5) and an assessment of post-volcanic cooling throughout the past 2,500 years using stacked tree-ring records and regional temperature reconstructions (Fig. 4, Extended Data Fig. 4) demonstrated that large eruptions in the tropics and high latitudes were primary drivers of interannual-to-decadal Northern Hemisphere temperature variability. The new ice-core chronologies imply that previous multi-proxy reconstructions of temperature that include ice-core records^{2–4} have diminished high- to mid-frequency amplitudes and must be updated to accurately capture the timing and full amplitude of palaeoclimatic variability.

By creating a volcanic forcing index independent of but consistent with tree-ring-indicated cooling, we provide an essential step towards understanding of external forcing on natural climate variability during the past 2,500 years. With the expected detection of additional rapid $\Delta^{14}\text{C}$ enrichment events from ongoing efforts in annual-resolution ¹⁴C tree-ring analyses⁴⁹, there will be opportunities to further constrain ice-core dating throughout the Holocene and develop a framework of precisely dated, globally synchronized proxies of past climate variability and external climate forcing.

Online Content Methods, along with any additional Extended Data display items and Source Data, are available in the online version of the paper; references unique to these sections appear only in the online paper.

Received 21 November 2014; accepted 6 May 2015.

Published online 8 July 2015.

1. Robock, A. Volcanic eruptions and climate. *Rev. Geophys.* **38**, 191–219 (2000).
2. Hanhijärvi, S., Tingley, M. P. & Korhola, A. Pairwise comparisons to reconstruct mean temperature in the Arctic Atlantic Region over the last 2,000 years. *Clim. Dyn.* **41**, 2039–2060 (2013).
3. PAGES 2k Consortium. Continental-scale temperature variability during the past two millennia. *Nature Geosci.* **6**, 503 (2013).
4. Mann, M. E. *et al.* Proxy-based reconstructions of hemispheric and global surface temperature variations over the past two millennia. *Proc. Natl Acad. Sci. USA* **105**, 13252–13257 (2008).
5. Usoskin, I. G. A history of solar activity over millennia. *Living Rev. Sol. Phys.* **10**, 1 (2013).
6. Gao, C. C., Robock, A. & Ammann, C. Volcanic forcing of climate over the past 1500 years: an improved ice core-based index for climate models. *J. Geophys. Res.* **113**, <http://dx.doi.org/10.1029/2008JD010239> (2008).
7. Crowley, T. J. & Unterman, M. B. Technical details concerning development of a 1200-yr proxy index of global volcanism. *Earth System Sci. Data* **5**, 187–197 (2013).
8. Mann, M. E., Fuentes, J. D. & Rutherford, S. Underestimation of volcanic cooling in tree-ring-based reconstructions of hemispheric temperatures. *Nature Geosci.* **5**, 202–205 (2012).
9. Mann, M. E., Rutherford, S., Schurer, A., Tett, S. F. B. & Fuentes, J. D. Discrepancies between the modeled and proxy-reconstructed response to volcanic forcing over the past millennium: implications and possible mechanisms. *J. Geophys. Res.* **118**, 7617–7627 (2013).
10. Schurer, A. P., Hegerl, G. C., Mann, M. E., Tett, S. F. B. & Phipps, S. J. Separating forced from chaotic climate variability over the past millennium. *J. Clim.* **26**, 6954–6973 (2013).

11. Anchukaitis, K. J. *et al.* Tree rings and volcanic cooling. *Nature Geosci.* **5**, 836–837 (2012).
12. Büntgen, U. *et al.* Extraterrestrial confirmation of tree-ring dating. *Nature Clim. Change* **4**, 404–405 (2014).
13. Esper, J., Büntgen, U., Luterbacher, J. & Krusic, P. J. Testing the hypothesis of post-volcanic missing rings in temperature sensitive dendrochronological data. *Dendrochronologia* **31**, 216–222 (2013).
14. D’Arrigo, R., Wilson, R. & Anchukaitis, K. J. Volcanic cooling signal in tree ring temperature records for the past millennium. *J. Geophys. Res.* **118**, 9000–9010 (2013).
15. Plummer, C. T. *et al.* An independently dated 2000-yr volcanic record from Law Dome, East Antarctica, including a new perspective on the dating of the 1450s CE eruption of Kuwae, Vanuatu. *Clim. Past* **8**, 1929–1940 (2012).
16. Sigl, M. *et al.* A new bipolar ice core record of volcanism from WAIS Divide and NEEM and implications for climate forcing of the last 2000 years. *J. Geophys. Res.* **118**, 1151–1169 (2013).
17. Sigl, M. *et al.* Insights from Antarctica on volcanic forcing during the Common Era. *Nature Clim. Change* **4**, 693–697 (2014).
18. Esper, J. *et al.* European summer temperature response to annually dated volcanic eruptions over the past nine centuries. *Bull. Volcanol.* **75**, 736 (2013).
19. Douglass, D. H. & Knox, R. S. Climate forcing by the volcanic eruption of Mount Pinatubo. *Geophys. Res. Lett.* **32**, L05710 (2005).
20. Baillie, M. G. L. Proposed re-dating of the European ice core chronology by seven years prior to the 7th century AD. *Geophys. Res. Lett.* **35**, L15813 (2008).
21. Baillie, M. G. L. & McAneney, J. Tree ring effects and ice core acidities clarify the volcanic record of the 1st millennium. *Clim. Past* **11**, 105–114 (2015).
22. Miyake, F., Nagaya, K., Masuda, K. & Nakamura, T. A signature of cosmic-ray increase in AD 774–775 from tree rings in Japan. *Nature* **486**, 240–242 (2012).
23. Miyake, F., Masuda, K. & Nakamura, T. Another rapid event in the carbon-14 content of tree rings. *Nature Commun.* **4**, <http://dx.doi.org/10.1038/Ncomms2783> (2013).
24. Usoskin, I. G. *et al.* The AD775 cosmic event revisited: the Sun is to blame. *Astron. Astrophys.* **552**, <http://dx.doi.org/10.1051/0004-6361/201321080> (2013).
25. Jull, A. J. T. *et al.* Excursions in the ¹⁴C record at A. D. 774–775 in tree rings from Russia and America. *Geophys. Res. Lett.* **41**, 3004–3010 (2014).
26. Gütler, D. *et al.* Rapid increase in cosmogenic ¹⁴C in AD 775 measured in New Zealand kauri trees indicates short-lived increase in ¹⁴C production spanning both hemispheres. *Earth Planet. Sci. Lett.* **411**, 290–297 (2015).
27. Miyake, F. *et al.* Cosmic ray event of AD 774–775 shown in quasi-annual ¹⁰Be data from the Antarctic Dome Fuji ice core. *Geophys. Res. Lett.* **42**, 84–89 (2015).
28. Webber, W. R., Higbie, P. R. & McCracken, K. G. Production of the cosmogenic isotopes H-3, Be-7, Be-10, and Cl-36 in the Earth’s atmosphere by solar and galactic cosmic rays. *J. Geophys. Res.* **112**, A10106 (2007).
29. Masarik, J. & Beer, J. An updated simulation of particle fluxes and cosmogenic nuclide production in the Earth’s atmosphere. *J. Geophys. Res.* **114**, D11103 (2009).
30. Vinther, B. M. *et al.* A synchronized dating of three Greenland ice cores throughout the Holocene. *J. Geophys. Res.* **111**, D13102 (2006).
31. Lavigne, F. *et al.* Source of the great A.D. 1257 mystery eruption unveiled, Samalás volcano, Rinjani Volcanic Complex, Indonesia. *Proc. Natl Acad. Sci. USA* **110**, 16742–16747 (2013).
32. Winstrup, M. *et al.* An automated approach for annual layer counting in ice cores. *Clim. Past* **8**, 1881–1895 (2012).
33. McCormick, M. *et al.* Climate change during and after the Roman Empire: reconstructing the past from scientific and historical evidence. *J. Interdisc. Hist.* **43**, 169–220 (2012).
34. Salzer, M. W. & Hughes, M. K. Bristlecone pine tree rings and volcanic eruptions over the last 5000 yr. *Quat. Res.* **67**, 57–68 (2007).
35. Esper, J., Duthorn, E., Krusic, P. J., Timonen, M. & Büntgen, U. Northern European summer temperature variations over the Common Era from integrated tree-ring density records. *J. Quat. Sci.* **29**, 487–494 (2014).
36. Crowley, T. J. Causes of climate change over the past 1000 years. *Science* **289**, 270–277 (2000).
37. Driscoll, S., Bozzo, A., Gray, L. J., Robock, A. & Stenchikov, G. Coupled Model Intercomparison Project 5 (CMIP5) simulations of climate following volcanic eruptions. *J. Geophys. Res.* **117**, D17105 (2012).
38. Schneider, D. P., Ammann, C. M., Otto-Bliessner, B. L. & Kaufman, D. S. Climate response to large, high-latitude and low-latitude volcanic eruptions in the Community Climate System Model. *J. Geophys. Res.* **114**, D15101 (2009).
39. Zanchettin, D. *et al.* Inter-hemispheric asymmetry in the sea-ice response to volcanic forcing simulated by MPI-ESM (COSMOS-Mil). *Earth Syst. Dyn.* **5**, 223–242 (2014).
40. Stothers, R. B. Mystery cloud of AD-536. *Nature* **307**, 344–345 (1984).
41. Larsen, L. B. *et al.* New ice core evidence for a volcanic cause of the AD 536 dust veil. *Geophys. Res. Lett.* **35**, L04708 (2008).
42. Büntgen, U. *et al.* 2500 years of European climate variability and human susceptibility. *Science* **331**, 578–582 (2011).
43. Esper, J. *et al.* Orbital forcing of tree-ring data. *Nature Clim. Change* **2**, 862–866 (2012).
44. D’Arrigo, R. *et al.* 1738 years of Mongolian temperature variability inferred from a tree-ring width chronology of Siberian pine. *Geophys. Res. Lett.* **28**, 543–546 (2001).
45. Zhang, Z. B. *et al.* Periodic climate cooling enhanced natural disasters and wars in China during AD 10–1900. *Proc. R. Soc. B* **277**, 3745–3753 (2010).
46. Stothers, R. B. Volcanic dry fogs, climate cooling, and plague pandemics in Europe and the Middle East. *Clim. Change* **42**, 713–723 (1999).

47. Stenseth, N. C. *et al.* Plague dynamics are driven by climate variation. *Proc. Natl Acad. Sci. USA* **103**, 13110–13115 (2006).
48. Dull, R. A. Evidence for forest clearance, agriculture, and human-induced erosion in Precolumbian El Salvador. *Ann. Assoc. Am. Geogr.* **97**, 127–141 (2007).
49. Taylor, R. E. & Southon, J. Reviewing the Mid-First Millennium BC C-14 “warp” using C-14/bristlecone pine data. *Nucl. Instrum. Meth. B* **294**, 440–443 (2013).

Supplementary Information is available in the online version of the paper.

Acknowledgements We thank the many people involved in logistics, drill development and drilling, and ice-core processing and analysis in the field and our laboratories. This work was supported by the US National Science Foundation (NSF). We appreciate the support of the WAIS Divide Science Coordination Office (M. Twickler and J. Souney) for collection and distribution of the WAIS Divide ice core; Ice Drilling and Design and Operations (K. Dahnert) for drilling; the National Ice Core Laboratory (B. Bencivengo) for curating the core; Raytheon Polar Services (M. Kippenhan) for logistics support in Antarctica; and the 109th New York Air National Guard for airlift in Antarctica. NEEM is directed and organized by the Center of Ice and Climate at the Niels Bohr Institute and the US NSF, Office of Polar Programs. It is supported by funding agencies and institutions in Belgium (FNRS-CFB and FWO), Canada (NRCan/GSC), China (CAS), Denmark (FIST), France (IPEV, CNRS/INSU, CEA and ANR), Germany (AWI), Iceland (Rannls), Japan (NIPR), Korea (KOPRI), The Netherlands (NWO/ALW), Sweden (VR), Switzerland (SNF), the UK (NERC), and the USA (the US NSF, Office of Polar Programs). We thank B. Nolan, O. Amir, K. D. Pang, M. McCormick, A. Matthews, and B. Rossignol for assistance in surveying and/or interpreting the historical evidence. We thank S. Kuehn for commenting on possible correlations for the tephra. We thank A. Aldahan and G. Possnert for their support in the NGRIP ¹⁰Be preparations and measurements at the Department of Earth Sciences and the Tandem laboratory at Uppsala University. We gratefully acknowledge R. Kreidberg for his editorial advice. The following individual grants supported this work: NSF/OPP grants 0839093, 0968391, and 1142166 to J.R.M. for development of the Antarctic ice core records and NSF/OPP grants 0909541,

1023672, and 1204176 to J.R.M. for development of the Arctic ice core records. M.W. was funded by the Villum Foundation. K.C.W. was funded by NSF/OPP grants 0636964 and 0839137. M.C. and T.E.W. were funded by NSF/OPP grants 0839042 and 0636815. F.L. was funded by the Yale Climate and Energy Institute, Initiative for the Science of the Human Past at Harvard, and the Rachel Carson Center for Environment and Society of the Ludwig-Maximilians-Universität (LMU Munich). C.K. was funded by a Marie Curie FP7 Integration Grant within the 7th European Union Framework Programme. M. Salzer was funded by NSF grant ATM 1203749. R.M. was funded by the Swedish Research Council (DNR2013-8421). The division of Climate and Environmental Physics, Physics Institute, University of Bern, acknowledges financial support by the SNF and the Oeschger Centre.

Author Contributions M. Sigl designed the study with input from J.R.M., M.W., G.P., and F.L. The manuscript was written by M. Sigl, M.W., F.L., and J.R.M., with contributions from K.C.W., G.P., U.B., and B.M.V. in interpretation of the measurements. Ice-core chemistry measurements were performed by J.R.M., M. Sigl, O.J.M., N.C., D.R.P. (NEEM, B40, TUNU2013), and by S.S., H.F., R. Mulvaney (NEEM). K.C.W., T.E.W., and M.C. completed ice core ¹⁰Be measurements. F.M. and R. Muscheler were responsible for the NGRIP ice core ¹⁰Be measurements. M. Sigl, M.W., B.M.V., and J.R.M. analysed ice-core data and developed age models. F.L. and C.K. analysed historical documentary data. G.P. and J.R.P. performed ice-core tephra analysis and data interpretation. U.B. and M. Salzer contributed tree-ring data. D.D.-J., B.M.V., J.P.S., S.K., and O.J.M. were involved in drilling of the NEEM ice core. TUNU2013 was drilled by M. Sigl, N.C. and O.J.M., and the B40 ice core was drilled by S.K. and made available for chemistry measurements. D.D.-J. and J.P.S. were responsible for NEEM project management, sample distribution, logistics support, and management. All authors contributed towards improving the final manuscript.

Author Information Reprints and permissions information is available at www.nature.com/reprints. The authors declare no competing financial interests. Readers are welcome to comment on the online version of the paper. Correspondence and requests for materials should be addressed to J.R.M. (joel.mcconnell@dri.edu).

METHODS

Ice cores. This study included new and previously described ice-core records from five drilling sites (Extended Data Fig. 1, Supplementary Data 1). The upper 577 m of the 3,405-m WAIS Divide (WDC) core from central West Antarctica and a 410-m intermediate-length core (NEEM-2011-S1) drilled in 2011 close to the 2,540-m North Greenland Eemian Ice Drilling (NEEM)⁵⁰ ice core have previously been used to reconstruct sulfate deposition in both polar ice sheets¹⁶. These coring sites are characterized by relatively high snowfall ($\sim 200 \text{ kg m}^{-2} \text{ yr}^{-1}$) and have comparable elevation, latitude, and deposition regimes. WDC and NEEM-2011-S1 provided high-resolution records that allowed annual-layer dating based on seasonally varying impurity content¹⁶. New ice-core analyses included the upper 514 m of the main NEEM core used to extend the record of NEEM-2011-S1 to cover the past 2,500 years, as well as B40 drilled in 2012 in Dronning Maud Land in East Antarctica and TUNU2013 drilled in 2013 in Northeast Greenland—both characterized by lower snowfall rates ($\sim 70\text{--}100 \text{ kg m}^{-2} \text{ yr}^{-1}$). Volcanic sulfate concentration from B40 had been reported previously for the past 2,000 years¹⁷, but we extended measurements to 200 m depth to cover the past 2,500 years.

High-resolution, ice-core aerosol analyses. Ice-core analyses were performed at the Desert Research Institute (DRI) using 55–100-cm-long, longitudinal ice-core sections (33 mm \times 33 mm wide). The analytical system for continuous analysis included two Element2 (Thermo Scientific) high-resolution inductively coupled plasma mass spectrometers (HR-ICP-MS) operating in parallel for measurement of a broad range of ~ 35 elements; an SP2 (Droplet Measurement Technologies) instrument for black carbon measurements; and a host of fluorimeters and spectrophotometers for ammonium (NH_4^+), nitrate (NO_3^-), hydrogen peroxide (H_2O_2), and other chemical species. All measurements were exactly co-registered in depth, with depth resolution typically less than 10–15 mm^{51–53}. We corrected total sulfur (S) concentrations for the sea-salt S contribution using sea-salt Na concentrations¹⁶. Measurements included TUNU2013 and NEEM (400–515 m) in Greenland, and B40 in Antarctica (Extended Data Fig. 1). Gaps (that is, ice not allocated to DRI) in the high-resolution sulfur data of the NEEM core were filled with ~ 4 -cm-resolution discrete sulfate measurements using fast ion-chromatography techniques⁵⁴ performed in the field between 428 m and 506 m depth.

Independent analyses of the upper part of the NEEM main core were performed in the field using a continuous flow analysis (CFA) system⁵⁵ recently modified to include a new melter head design⁵⁶. Ca^{2+} , NH_4^+ , and H_2O_2 were analysed by fluorescence spectroscopy; Na^+ and NO_3^- by absorption spectroscopy; conductivity of the meltwater by a micro flow cell (Amber Science); and a particle detector (Abakus, Klotz) was used for measuring insoluble dust particle concentrations and size distribution⁵⁷. Effective depth resolution was typically better than 20 mm. Measurements were exactly synchronized in depth using a multicomponent standard solution; the accuracy of the depth assignment for all measurements was typically better than 5 mm.

High-resolution measurements of ^{10}Be in ice cores using AMS. Accelerator mass spectrometry (AMS) was used to analyse samples from the NEEM-2011-S1, WDC, NGRIP, and TUNU2013 ice cores encompassing the time period of the $\Delta^{14}\text{C}$ anomalies from tree-ring records^{12,22–25} were used for ^{10}Be analysis (Supplementary Data 1). NEEM-2011-S1 and WDC were sampled in exact annual resolution, using the maxima (minima in WDC) of the annual cycles of Na concentrations to define the beginning of the calendar year¹⁶. NGRIP was sampled at a constant resolution of 18.3 cm, providing an age resolution of about one year. Similarly, TUNU2013 was sampled in quasi-annual resolution according to the average annual-layer thickness expected at this depth based on prior volcanic synchronization to NEEM-2011-S1. The relative age uncertainty for TUNU2013 with respect to the dependent NEEM-2011-S1 chronology at this depth is assumed to be ± 1 year at most, given a distinctive match for selected volcanic trace elements in both ice-core records (752–764 CE, NS1-2011 timescale). Sample masses ranged between 100 g and 450 g, resulting in median overall quantification uncertainties of less than 4%–7%. The $^{10}\text{Be}/^9\text{Be}$ ratios of samples and blanks were measured relative to well documented ^{10}Be standards¹³ by AMS at Purdue's PRIME laboratory (WDC, NEEM-2011-S1, TUNU2013) and Uppsala University (NGRIP)^{58,59}. Results were corrected for an average blank $^{10}\text{Be}/^9\text{Be}$ ratio, corresponding to corrections of 2%–10% of the measured $^{10}\text{Be}/^9\text{Be}$ ratios.

Annual-layer dating using the StratiCounter algorithm. For annual-layer interpretation, we used DRI's broad-spectrum aerosol concentration data from WDC (188–577 m), NEEM-2011-S1 (183–411 m), and NEEM (410–515 m), as well as NEEM aerosol concentration data (183–514 m) from the field-based CFA system. The original timescale for NEEM-2011-S1 was based on volcanic synchronization to the NGRIP sulfate record on the GICC05 timescale and annual-layer interpretation between the volcanic age markers, whereas WDC was previously dated by annual-layer counting¹⁶.

Parameters with strong intra-annual variability included tracers of sea salt (for example, Na, Cl, Sr), dust (for example, Ce, Mg, insoluble particle concentration), and marine biogenic emissions such as non-sea-salt sulfur (nssS). Tracers of biomass-burning emissions, such as BC, NH_4^+ , and NO_3^- , also showed strong seasonal variations in deposition during pre-industrial times^{16,60,61}. The data sets used for annual-layer interpretation are provided in Extended Data Table 1. For NEEM-2011-S1, the final database used for annual-layer dating included 13 parameters and the ratio of nssS/Na. For WDC, the final database included five parameters and the ratio of nssS/Na. For NEEM (410–515 m depth), the final database included eight parameters (Na^+ , Ca^{2+} , NH_4^+ , H_2O_2 , NO_3^- , conductivity, insoluble particle concentrations, and electrical conductivity⁶²) from the field-based measurements and eleven parameters (Na, Cl, Mg, Mn, Sr, nssS, nssS/Na, nssCa, black carbon, NO_3^- , NH_4^+) from the DRI system.

We focused here on the time period before the large volcanic eruption of Samalas in 1257 CE³¹, clearly detectable as an acidic peak in both ice-core records, and consequently started annual-layer counting of NEEM-2011-S1, NEEM, and WDC at the depth of the corresponding sulfur signal. For the time period 1257 CE to present, ice-core chronologies were constrained by numerous historic eruptions and large sulfate peaks, showing a strong association to Northern Hemisphere cooling events as indicated by tree-ring records¹⁶.

We applied the StratiCounter layer-detection algorithm³² to the multi-parameter aerosol concentration records ($n = 14$ for NEEM-2011-S1; $n = 6$ for WDC; $n = 8$ for NEEM < 410 m; $n = 19$ for NEEM > 410 m) to objectively determine the most likely number of annual layers in the ice cores along with corresponding uncertainties. The StratiCounter algorithm is based on statistical inference in Hidden Markov Models (HMMs), and it determines the maximum-likelihood solution based on the annual signal in all aerosol records in parallel. Some of these displayed a high degree of similarity, so we weighted these records correspondingly lower. The algorithm was run step-wise down the core, each batch covering approximately 50 years, with a slight overlap. All parameters for the statistical description of a mean layer and its inter-annual variability in the various aerosol records were determined independently for each batch as the maximum-likelihood solution. The algorithm simultaneously computes confidence intervals for the number of layers within given sections, allowing us to provide uncertainty bounds on the number of layers between selected age-marker horizons (Extended Data Table 2).

Annual-layer detection in the NEEM main core below 410 m was made more difficult by frequent occurrence of small gaps in the two independent high-resolution aerosol data sets. Depending on the parameter, data gaps from the CFA field measurements accounted for up to 20% of the depth range between 410 m and 515 m, but the combined aerosol records from both analyses provided an almost complete aerosol record with 96% data coverage. As this was the first time that the StratiCounter algorithm was used simultaneously on data records from two different melt systems, with different characteristics and lack of exact co-registration, we also manually determined annual layers below 410 m using the following approaches: one investigator used Na and nssCa concentrations and the ratio of nssS/Na (from DRI analysis) as well as Na^+ and insoluble particle concentrations (from CFA analysis) as primary dating parameters. Black carbon, NH_4^+ , nssS, and conductivity were used as secondary dating parameters where annual-layer interpretation was ambiguous. A second investigator used DRI's Na, Ca, BC, NH_4^+ and CFA Na^+ , Ca^{2+} , and NH_4^+ measurements as parameters. The annual-layer interpretation of the NEEM core between 410 m and 514 m from investigator 1 was within the interpretation uncertainties of the StratiCounter output, from which it differed by less than a single year over the majority of this section, and it differed from independently counted timescales (for example, GICC05)⁶² by on average less than three years (Extended Data Fig. 2). This set of layer counts was used for the resulting timescale.

New ice-core chronologies for NS1-2011 and WD2014. We defined the depth of NEEM-2011-S1 containing the maximum ^{10}Be concentration as the year 775 CE. Relative to this constraint, the maximum-likelihood ages for three large volcanic sulfate peaks were within one year of documented historical reports from early written sources of prominent and sustained atmospheric dimming observed in Europe and/or the Near East (Extended Data Table 3, Supplementary Data 2). Automated-layer identification for NEEM-2011-S1 was therefore constrained by tying the respective ice-core volcanic signals to the corresponding absolute historically dated ages of 536 CE, 626 CE, and 939 CE (Extended Data Table 2)—thereby creating a new ice-core timescale (NS1-2011). The volcanic sulfur signal corresponding to the eruption of Samalas believed to have occurred in late 1257³¹ was constrained to 1258 CE to account for several months' delay in sulfate deposition in the high latitudes. Before 86 CE (the bottom depth of NEEM-2011-S1), the NS1-2011 timescale was extended using the manually derived annual-layer interpretation of the combined NEEM aerosol data sets back to 500 BCE (Fig. 2).

In NS1-2011 we did not attribute acid layers to the historical eruptions Vesuvius 79 and Hekla 1104, due to a lack of corroborative tephra at these depths in this and a previous study⁶³. Possible Vesuvian tephra was reported from the Greenland Ice Sheet Project (GRIP) ice core at 429.3 m depth⁶⁴, but in view of the new annual-layer dating results (Extended Data Fig. 3), we concluded that this layer dates to 87/88 CE. Furthermore, volcanic sulfate deposition values for the corresponding event show a strong spatial gradient over Greenland with highest values in north-west Greenland¹⁶ and lowest in central and south Greenland⁶⁵, favouring the attribution of a volcanic source from the high latitudes. Documentary sources (Supplementary Data 2) also suggest that the main vector of ash transport following the Vesuvius 79 CE eruption was towards the eastern Mediterranean⁶⁶.

For WDC, we do not have other sufficiently well determined age constraints besides the rapid ¹⁰Be increase in 775 CE and the sulfur signal of the Samalas 1257 eruption. Therefore, no additional constraints were used when creating the new ice-core timescale ("WD2014") from the StratiCounter annual-layer interpretation back to 396 BCE.

Depth-age information for six distinctive marker horizons in Greenland is given, and five of these horizons were used to constrain NS1-2011 (Extended Data Table 3). Similarly, depth information, the number of annual layers, and 95% confidence intervals between distinctive volcanic marker horizons are given for NEEM, NEEM-2011-S1, and WDC, supporting attribution of these ice-core signals to eruptions in the low latitudes with bipolar sulfate deposition.

Evaluation of NS1-2011 using independent age information. We evaluated timescale accuracy using additional distinctive age markers not used during chronology development:

(1) Tephra from the eruption of Changbaishan/Tianchi (China)⁶⁷ was detected in NEEM-2011-S1 in 946–947 CE, in agreement with widespread documentary evidence of an eruption in that region in winter 946/47 CE⁶⁸ also supported by a high-precision ¹⁴C wiggle-match age of 946 ± 3 CE obtained from a tree killed during this eruption⁶⁸.

(2) The rapid increase of ¹⁰Be from the 994 CE event occurred in NEEM-2011-S1 in 993 CE, consistent with $\Delta^{14}\text{C}$ from Japanese tree rings showing that the rapid increase in radionuclide production took place between the Northern Hemisphere growing seasons of 993 CE and 994 CE²³.

(3) To assess the accuracy of the NS1-2011 timescale before the earliest age marker at 536 CE, we compiled an independent time series of validation points, featuring years with well dated historical reports of atmospheric phenomena associated with high-altitude volcanic dust and/or aerosols (Supplementary Data 2) as known from modern observations to occur after major eruptions (for example, the Krakatau eruption of 1883). These phenomena include diminished sunlight, discoloration of the solar disk, solar coronae (that is, Bishop's Rings), and deeply red twilights (that is, volcanic sunsets)^{69,70}. Thirty-two events met our criteria as validation points for the pre-536 CE NS1-2011 timescale. For the earliest in 255 BCE, it was reported in Babylon that "the disk of the sun looked like that of the moon"⁷¹. For the latest in 501 CE, it was reported in North China that "the Sun was red and without brilliance"⁷². We found that NEEM volcanic event years (including both NEEM and NEEM-2011-S1 data) occurred closely in time (that is, within a conservative ±3-year margin) to 24 (75.0%) of our validation points (Extended Data Fig. 2). To assess whether this association arose solely by chance, we conducted a Monte Carlo equal means test with 1,000,000 iterations (Supplementary Data 2) and found that the number of volcanic event years within three years of our validation points was significantly greater than expected randomly ($P < 0.001$). A significant association was also observed ($P < 0.001$) when using less conservative error margins (±1 and ±2 years) and when excluding any historical observations with less certainty of a volcanic origin (Supplementary Data 2). When placing volcanic event years on the original GICC05 timescale, we did not observe any statistically significant association with our independent validation points.

Potential causes of a previous ice-core dating bias. Interpretation of annual layers in ice cores is subject to accumulating age uncertainty due to ambiguities in the underlying ice-core profiles^{30,73}. Bias in existing chronologies may arise from several factors, including: (1) low effective resolution of some ice-core measurements (NGRIP, GRIP); (2) use of only single (or few) parameters for annual-layer interpretation (GRIP, Dye-3 ice cores); (3) intra-annual variations in various ice-core parameters falsely interpreted as layer boundaries (for example, caused by summer melt in Dye-3)⁷⁴; (4) use of tephra believed to originate from the 79 CE Vesuvian eruption⁶⁴ as a fixed reference horizon to constrain the Greenland ice-core dating³⁰; (5) use of manual-layer interpretation techniques that may favour interpretations consistent with a priori knowledge or existing chronologies (WDC)^{16,21}.

Volcanic synchronization of B40, TUNU2013, and NGRIP. Two high-resolution sulfur ice-core records (TUNU2013, Greenland and B40, Antarctica) were synchronized to NEEM-2011-S1 and WDC, respectively, using volcanic stratigraphic

age markers¹⁷ with relative age uncertainty between the tie-points estimated to not exceed ±2 years. The NGRIP sulfate record measured at 5 cm depth resolution¹⁵ similarly was synchronized to NS1-2011 using 124 volcanic tie-points between 226 and 1999 CE. During the time period with no sulfur record yet available for WDC (before 396 BCE), a tentative chronology for B40 was derived by linearly extrapolating mean annual-layer thickness for B40 as derived from the synchronization to WDC between the earliest volcanic match points.

2,500 year global volcanic forcing ice-core index. We constructed an index of global volcanic aerosol forcing by (1) re-dating and extending to 500 BCE an existing reconstruction of sulfate flux from an Antarctic ice-core array¹⁷ by applying an area weighting of 80/20 between East Antarctica and West Antarctica to B40 and WDC volcanic sulfate flux values, respectively; (2) compositing NGRIP and the NEEM-2011-S1/NEEM sulfate flux records to a similar Greenland sulfate deposition composite back to 500 BCE; (3) using established scaling functions^{6,75} to estimate hemispheric sulfate aerosol loading from both polar ice-core composites; and (4) scaling global aerosol loading to the total (that is, time-integrated) radiative volcanic aerosol forcing following the Tambora 1815 eruption⁷. Since the NS1-2011 and WD2014 timescales are independent of each other, the timing of bipolar events had to be adjusted to follow a single timescale to derive a unified global volcanic forcing series. We chose NS1-2011 as the reference chronology for most of the volcanic time series because this age model was constrained and validated by more stratigraphic age markers than WD2014. WD2014 was used as the reference chronology only between 150 CE and 450 CE, because of better data quality during that time period. TUNU2013 was not included in the Greenland ice-core composite because annual-layer thickness variability at this site is influenced strongly by glaciological processes, leading to relatively large uncertainties in atmospheric sulfur-deposition determinations.

Northern Hemisphere tree-ring composite. Tree-ring records from certain locations reflect summer cooling (as is widely observed after volcanic eruptions) with no age uncertainty in annual ring-width dating, thus allowing independent validation of ice-core timescales and the derived volcanic forcing indices. However, no tree-ring-based temperature reconstructions of large spatial scales span the full 2,500 years represented by our new ice-core chronologies. To thus evaluate our new ice-core chronologies and assess the consistency of response throughout the past 2,500 years, we compiled a composite (entitled 'N-Tree') of multi-centennial tree growth records at locations where temperature is the limiting growth factor. We selected available Northern Hemisphere tree-ring records that provided a continuous record of >1,500 years and showed a significant positive relationship with JJA temperatures during the instrumental period (1901–2000 CE) with $P < 0.005$ (adjusted for a reduced sample size owing to autocorrelation of the data sets). In total, five tree-ring chronologies (three based on ring-width measurements, two based on measurements of maximum late-wood density) met these criteria^{42,43,76–78} of which three are located in the high latitudes of Eurasia (Extended Data Fig. 1).

As various climatic and non-climatic parameters may influence sensitivity of tree growth to temperatures during the twentieth century^{79–81}, we used the time period 1000–1099 CE as a common baseline for standardizing tree growth anomalies among the five chronologies and built a tree growth composite record called N-Tree (z -scores) by averaging the individual records. Correlations between N-Tree ($N = 5$) and the average of three regional reconstructions for the Arctic, Europe, and Asia ($N > 275$)³ between 1800 CE and 2000 CE are very high ($r = 0.86$, $N = 201$, $P < 0.0001$), suggesting that much of the large-scale variation in temperature is explained by these selected tree-ring records. Three records in N-Tree cover the period from 138 BCE to the present, thus allowing at least a qualitative assessment of the coherence of growth reduction following large volcanic eruptions before the Common Era (Fig. 2, Extended Data Fig. 4).

Temperature reconstructions. To quantify the Common Era climate impact and investigate regional differences, we used tree-ring-based JJA temperature reconstructions covering the past 2,000 years with a demonstrated strong relationship ($r \geq 0.45$; $P < 0.0001$; Extended Data Fig. 1) to instrumental JJA temperature data⁸² between 1901 and 2000. For regions where this criterion was met by several reconstructions (for example, Scandinavia), we limited the analysis to the most recently updated reconstruction³⁵. Three regional reconstructions from Central Europe⁴², Northern Europe³⁵, and Northern Siberia (Yamal, not shown)⁷⁶ as well as a continental-scale reconstruction for Europe³ met this criterion and were used to quantify the average response of summer temperature to volcanic forcing during the Common Era (Figs 3 and 4).

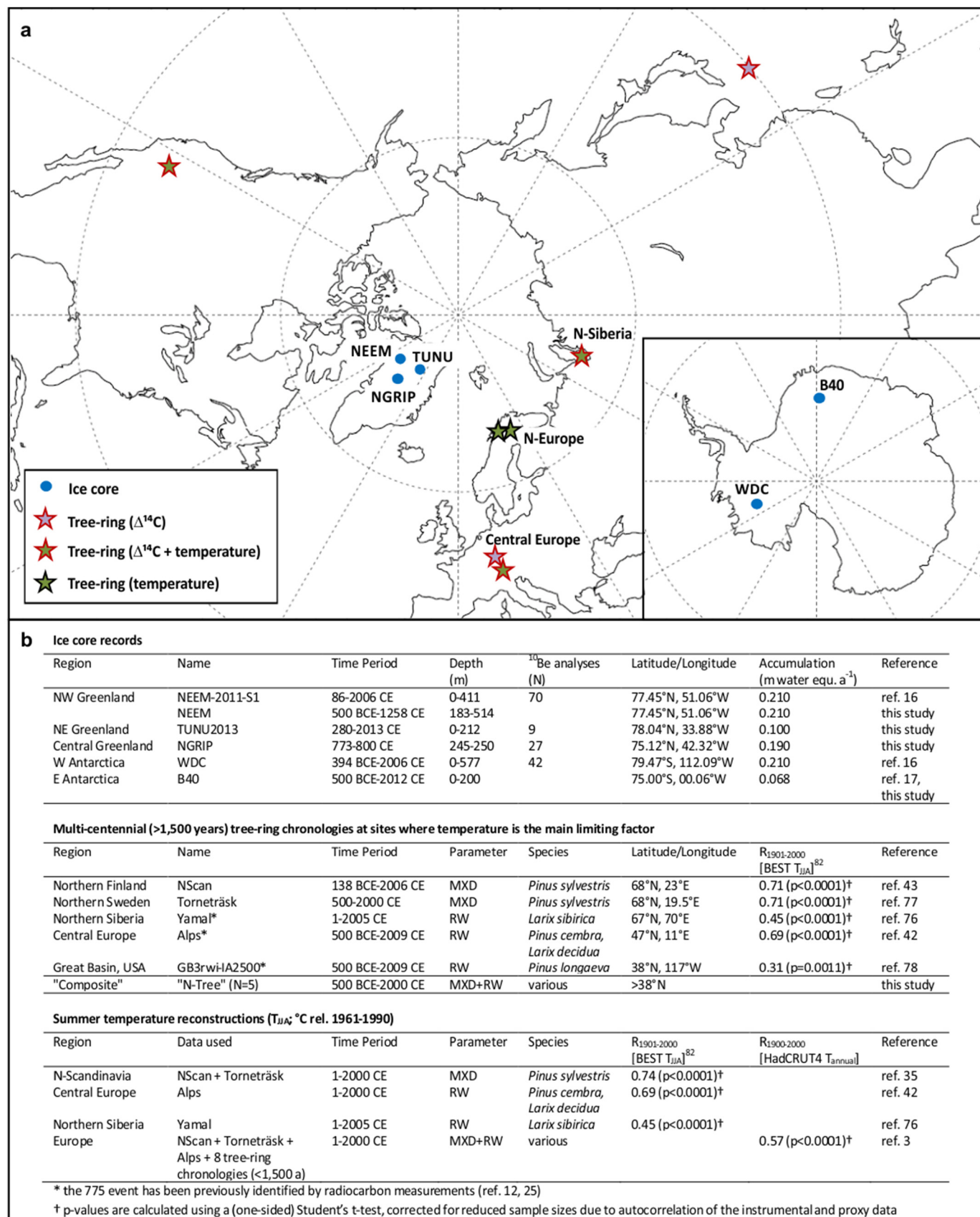
Superposed epoch analyses. To assess tree-ring growth reduction and summer cooling following large eruptions, we used superposed epoch analyses^{83,84}. We selected all volcanic eruptions (28 events in total, 24 CE events) with time-integrated volcanic forcing greater than -7.5 W m^{-2} (that is, eruptions larger than Pinatubo 1991) and aligned the individual segments of N-Tree and regional

JJA temperature reconstructions relative to ice-core-indicated peak forcing. The composite response was calculated for the average of the individual series (lag 0 to lag 10 or 15 years) relative to the average values five years before individual volcanic events (lag -5 to lag -1 year). 95% confidence intervals represent 2 s.e.m. of the tree-growth (Extended Data Fig. 4) and temperature anomalies (Fig. 4) associated with the multiple eruptions.

Cryptotephra analyses of the 536 CE sample from NEEM-2011-S1. We analysed samples from NEEM-2011-S1 for tephra between 326.73 m and 328.06 m depth, corresponding to 531–539 CE (NS1-2011 timescale). Samples (200 g to 500 g) were filtered, and elemental composition of recovered volcanic glass shards determined by electron microprobe analysis at Queen's University Belfast using established protocols^{63,67,85} and secondary glass standards^{86,87}. Between 326.73 m and 327.25 m, large volume samples were cut at 8 cm depth resolution (≤ 0.5 years) and with an average cross-section of 26 cm². Between 327.25 m and 328.06 m, the average cross-section was 7 cm² and depth resolution 20 cm (~ 1 yr resolution). Tephra particles ($n \geq 17$) were isolated from a sample of ice (327.17–327.25 m depth, 251 g) corresponding to the sulfate spike at 536 CE. The glass shards were heterogeneous in size (20–80 μm), morphology (platey, blocky, vesicular, microlitic), and geochemistry (andesitic, trachytic, rhyolitic). Individual shards had geochemical compositions that share affinities with volcanic systems in the Aleutian arc (Alaska)⁸⁸, Northern Cordilleran volcanic province (British Columbia)⁸⁹, and Mono-Inyo Craters area (California)^{90,91}—indicating at least three synchronous eruptive events, all situated in western North America between 38°N and 58°N (Extended Data Fig. 5; Supplementary Data 5).

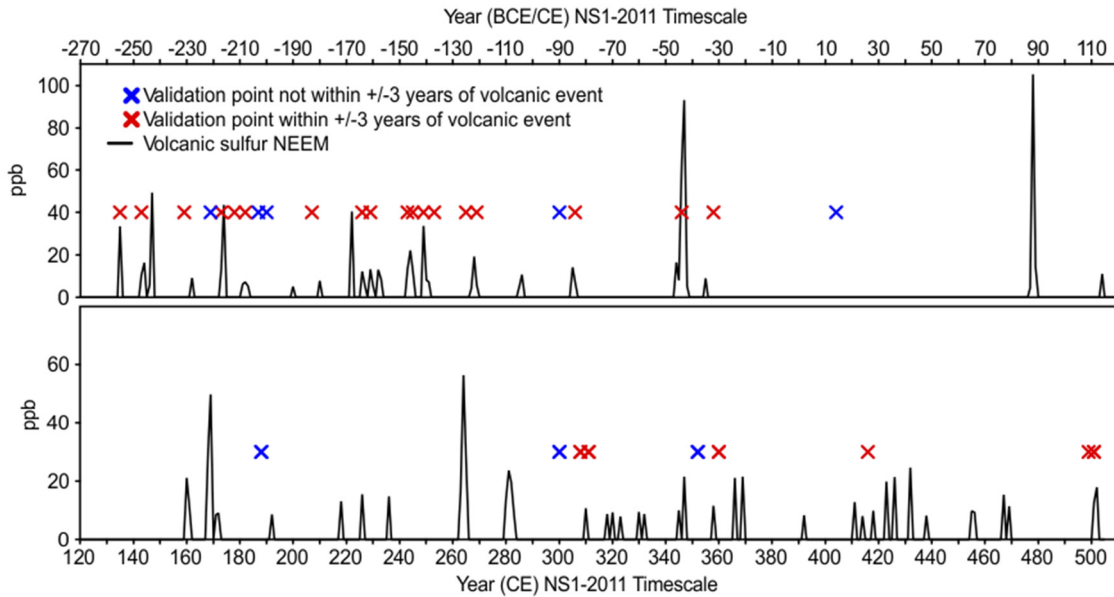
Data and code availability. Ice-core data (chemistry, including sulphur and ¹⁰Be), the resulting timescales, and the volcanic forcing reconstruction are provided as Supplementary Data 1, and 3–5. Historical documentary data are provided as Supplementary Data 2. The code for the StratiCounter program is accessible at the github repository (<http://www.github.com/maiwinsturp/StratiCounter>). NGRIP SO₄ data can be obtained at http://www.iceandclimate.nbi.ku.dk/data/2012-12-03_NGRIP_SO4_5cm_Plummet_et_al_CP_2012.txt. Tree-ring records and temperature reconstructions are from the Supplementary Database S1 and S2 of the Pages-2k Consortium (ref. 3; <http://www.nature.com/ngeo/journal/v6/n5/full/ngeo1797.html#supplementary-information>).

50. Dahl-Jensen, D. *et al.* Eemian interglacial reconstructed from a Greenland folded ice core. *Nature* **493**, 489–494 (2013).
51. McConnell, J. R. Continuous ice-core chemical analyses using inductively coupled plasma mass spectrometry. *Environ. Sci. Technol.* **36**, 7–11 (2002).
52. McConnell, J. R. & Edwards, R. Coal burning leaves toxic heavy metal legacy in the Arctic. *Proc. Natl Acad. Sci. USA* **105**, 12140–12144 (2008).
53. Pasteris, D. R. *et al.* Seasonally resolved ice core records from West Antarctica indicate a sea ice source of sea-salt aerosol and a biomass burning source of ammonium. *J. Geophys. Res.* **119**, 9168–9182 (2014).
54. Abram, N. J., Mulvaney, R. & Arrowsmith, C. Environmental signals in a highly resolved ice core from James Ross Island, Antarctica. *J. Geophys. Res.* **116**, D20116 (2011).
55. Kaufmann, P. R. *et al.* An improved continuous flow analysis system for high-resolution field measurements on ice cores. *Environ. Sci. Technol.* **42**, 8044–8050 (2008).
56. Bigler, M. *et al.* Optimization of High-Resolution Continuous Flow Analysis for Transient Climate Signals in Ice Cores. *Environ. Sci. Technol.* **45**, 4483–4489 (2011).
57. Ruth, U., Wagenbach, D., Steffensen, J. P. & Bigler, M. Continuous record of microparticle concentration and size distribution in the central Greenland NGRIP ice core during the last glacial period. *J. Geophys. Res.* **108** (2003).
58. Woodruff, T. E., Welten, K. C., Caffee, M. W. & Nishiizumi, K. Interlaboratory comparison of Be-10 concentrations in two ice cores from Central West Antarctica. *Nucl. Instrum. Meth. B* **294**, 77–80 (2013).
59. Berggren, A. M. *et al.* Variability of Be-10 and delta O-18 in snow pits from Greenland and a surface traverse from Antarctica. *Nucl. Instrum. Meth. B* **294**, 568–572 (2013).
60. Bisiaux, M. M. *et al.* Changes in black carbon deposition to Antarctica from two high-resolution ice core records, 1850–2000 AD. *Atmos. Chem. Phys.* **12**, 4107–4115 (2012).
61. Pasteris, D., McConnell, J. R., Edwards, R., Isaksson, E. & Albert, M. R. Acidity decline in Antarctic ice cores during the Little Ice Age linked to changes in atmospheric nitrate and sea salt concentrations. *J. Geophys. Res.* **119**, 5640–5652 (2014).
62. Rasmussen, S. O. *et al.* A first chronology for the North Greenland Eemian Ice Drilling (NEEM) ice core. *Clim. Past* **9**, 2713–2730 (2013).
63. Coulter, S. E. *et al.* Holocene tephras highlight complexity of volcanic signals in Greenland ice cores. *J. Geophys. Res.* **117**, D21303 (2012).
64. Barbante, C. *et al.* Greenland ice core evidence of the 79 AD Vesuvius eruption. *Clim. Past* **9**, 1221–1232 (2013).
65. Clausen, H. B. *et al.* A comparison of the volcanic records over the past 4000 years from the Greenland Ice Core Project and Dye 3 Greenland Ice Cores. *J. Geophys. Res.* **102**, 26707–26723 (1997).
66. Rolandi, G., Paone, A., Di Lascio, M. & Stefani, G. The 79 AD eruption of Somma: the relationship between the date of the eruption and the southeast tephra dispersion. *J. Volcanol. Geotherm. Res.* **169**, 87–98 (2008).
67. Sun, C. Q. *et al.* Ash from Changbaishan millennium eruption recorded in Greenland ice: implications for determining the eruption's timing and impact. *Geophys. Res. Lett.* **41**, 694–701 (2014).
68. Xu, J. D. *et al.* Climatic impact of the millennium eruption of Changbaishan volcano in China: new insights from high-precision radiocarbon wiggle-match dating. *Geophys. Res. Lett.* **40**, 54–59 (2013).
69. Deirmendjian, D. On volcanic and other particulate turbidity anomalies. *Adv. Geophys.* **16**, 267–296 (1973).
70. Vollmer, M. Effects of absorbing particles on coronas and glories. *Appl. Opt.* **44**, 5658–5666 (2005).
71. Sachs, A. J. & Hunger, H. *Astronomical Diaries and Related Texts from Babylonia* Vol.3 *Diaries from 164 B.C. to 61 B.C.* (Verlag der Österreichischen Akademie der Wissenschaften, 1996).
72. Wittmann, A. D. & Xu, Z. T. A catalog of sunspot observations from 165 BC to AD 1684. *Astron. Astrophys. (Suppl.)* **70**, 83–94 (1987).
73. Rasmussen, S. O. *et al.* A new Greenland ice core chronology for the last glacial termination. *J. Geophys. Res.* **111**, D06102 (2006).
74. Herron, M. M., Herron, S. L. & Langway, C. C. Climatic signal of ice melt features in southern Greenland. *Nature* **293**, 389–391 (1981).
75. Gao, C. H., Oman, L., Robock, A. & Stenchikov, G. L. Atmospheric volcanic loading derived from bipolar ice cores: accounting for the spatial distribution of volcanic deposition. *J. Geophys. Res.* **112**, D09109 (2007).
76. Briffa, K. R. *et al.* Reassessing the evidence for tree-growth and inferred temperature change during the Common Era in Yamalia, northwest Siberia. *Quat. Sci. Rev.* **72**, 83–107 (2013).
77. Grudd, H. Tornetrask tree-ring width and density AD 500–2004: a test of climatic sensitivity and a new 1500-year reconstruction of north Fennoscandian summers. *Clim. Dyn.* **31**, 843–857 (2008).
78. Salzer, M. W., Bunn, A. G., Graham, N. E. & Hughes, M. K. Five millennia of paleotemperature from tree-rings in the Great Basin, USA. *Clim. Dyn.* **42**, 1517–1526 (2014).
79. McMahon, S. M., Parker, G. G. & Miller, D. R. Evidence for a recent increase in forest growth. *Proc. Natl Acad. Sci. USA* **107**, 3611–3615 (2010).
80. Salzer, M. W., Hughes, M. K., Bunn, A. G. & Kipfmüller, K. F. Recent unprecedented tree-ring growth in bristlecone pine at the highest elevations and possible causes. *Proc. Natl Acad. Sci. USA* **106**, 20348–20353 (2009).
81. Briffa, K. R. *et al.* Reduced sensitivity of recent tree-growth to temperature at high northern latitudes. *Nature* **391**, 678–682 (1998).
82. Rohde, R. *et al.* A new estimate of the average land surface temperature spanning 1753 to 2011. *Geoinform. Geostat. Overview* **1**, <http://dx.doi.org/10.4172/2327-4581.1000101> (2013).
83. Mass, C. F. & Portman, D. A. Major volcanic eruptions and climate: a critical evaluation. *J. Clim.* **2**, 566–593 (1989).
84. Fritts, H. C., Lofgren, G. R. & Gordon, G. A. Variations in climate since 1602 as reconstructed from tree rings. *Quat. Res.* **12**, 18–46 (1979).
85. Jensen, B. J. L. *et al.* Transatlantic distribution of the Alaskan White River Ash. *Geology* **42**, 875–878 (2014).
86. Oskarsson, N., Sigvaldason, G. E. & Steinthorsson, S. A dynamic-model of rift-zone petrogenesis and the regional petrology of Iceland. *J. Petrol.* **23**, 28–74 (1982).
87. Kuehn, S. C., Froese, D. G., Shane, P. A. R. & Participants, I. I. The INTAV intercomparison of electron-beam microanalysis of glass by tephrochronology laboratories: results and recommendations. *Quat. Int.* **246**, 19–47 (2011).
88. Kaufman, D. S. *et al.* Late Quaternary tephrostratigraphy, Ahklun mountains, SW Alaska. *J. Quat. Sci.* **27**, 344–359 (2012).
89. Lakeman, T. R. *et al.* Holocene tephras in lake cores from northern British Columbia, Canada. *Can. J. Earth Sci.* **45**, 935–947 (2008).
90. Bursik, M., Sieh, K. & Meltzner, A. Deposits of the most recent eruption in the Southern Mono Craters, California: description, interpretation and implications for regional marker tephras. *J. Volcanol. Geotherm. Res.* **275**, 114–131 (2014).
91. Sampson, D. E. & Cameron, K. L. The geochemistry of the Inyo volcanic chain—multiple magma systems in the Long Valley region, eastern California. *J. Geophys. Res.* **92**, 10403–10421 (1987).
92. Veres, D. *et al.* The Antarctic ice core chronology (AICC2012): an optimized multi-parameter and multi-site dating approach for the last 120 thousand years. *Clim. Past* **9**, 1733–1748 (2013).
93. Siebert, L., Simkin, T. & Kimberly, P. *Volcanoes of the World* 3rd edn, (University of California Press, 2010).



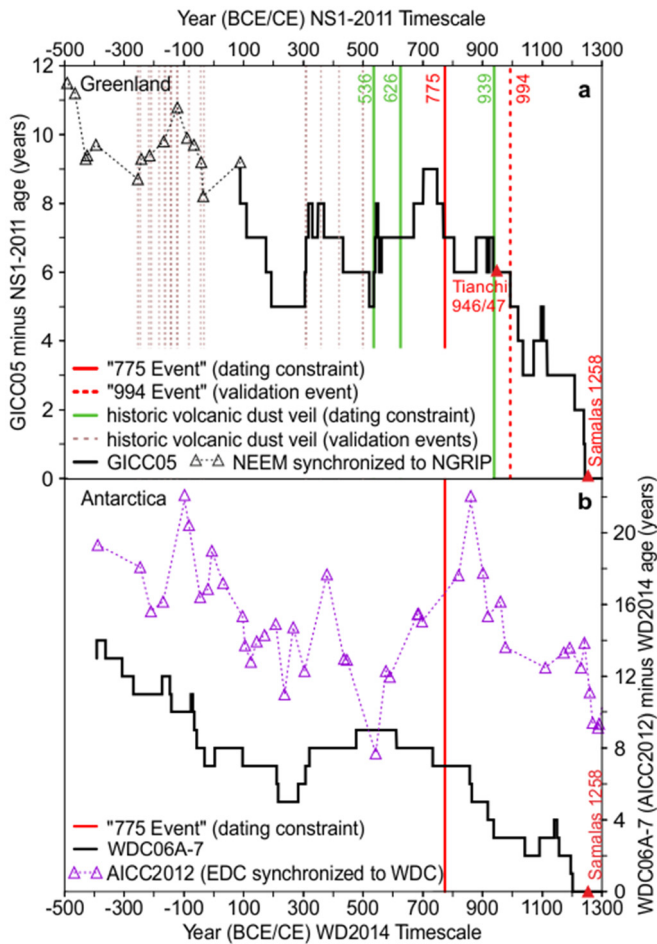
Extended Data Figure 1 | Location of study sites. **a**, Map showing locations (blue circles) of the five ice cores (WDC, B40, NEEM, NGRIP and TUNU) used in this study. Sites of temperature-limited tree-ring chronologies (green)^{42,43,76-78} and sites with annual $\Delta^{14}\text{C}$ measurements from tree-rings in

the eighth century CE (red outline) are marked. **b**, Metadata for the ice cores, tree-ring width (RW), maximum latewood density (MXD) chronologies and temperature reconstructions used^{13,12,16,17,25,35,42,43,76,77,78,82}. m water equ. a⁻¹, metres of water equivalent per year.

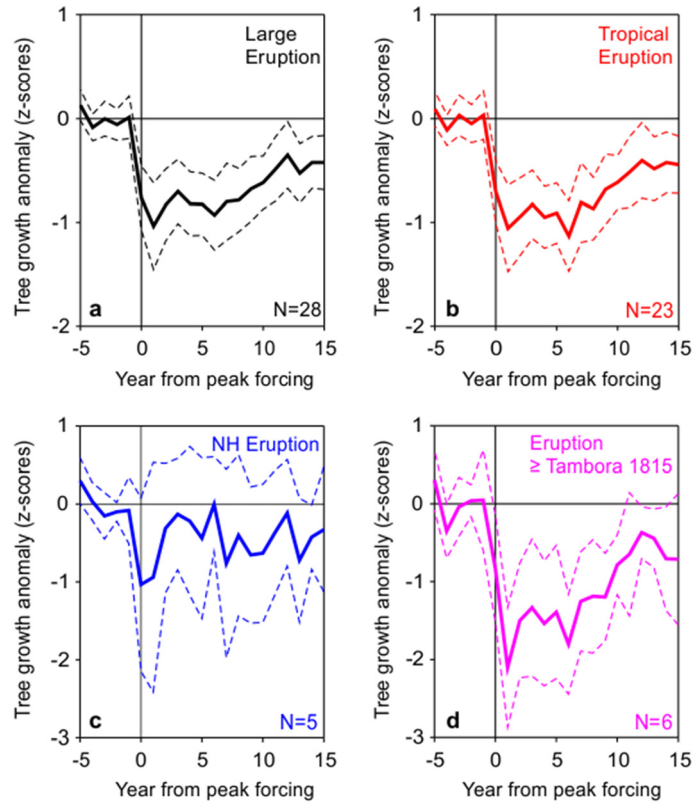


Extended Data Figure 2 | Volcanic dust veils from historical documentary sources in relation to NEEM. Time series of 32 independently selected chronological validation points from well dated historical observations of atmospheric phenomena with known association to explosive volcanism (for example, diminished sunlight, discoloured solar disk, solar corona or Bishop's Ring, red volcanic sunset) as reported in the Near East, Mediterranean region, and China, before our earliest chronological age marker at 536 CE. Black lines represent the magnitude (scale on *y* axes) of annual sulfate deposition

measured in NEEM (NEEM and NEEM-2011-S1 ice cores) from explosive volcanic events on the new NS1-2011 timescale. Red crosses depict the 24 (75%) historical validation points for which NEEM volcanic events occur within a conservative ± 3 -year uncertainty margin. Blue crosses represent the eight points for which volcanic events are not observed. The association between validation points and volcanic events is statistically significantly non-random at $>99.9\%$ confidence ($P < 0.001$). ppb, parts per billion.



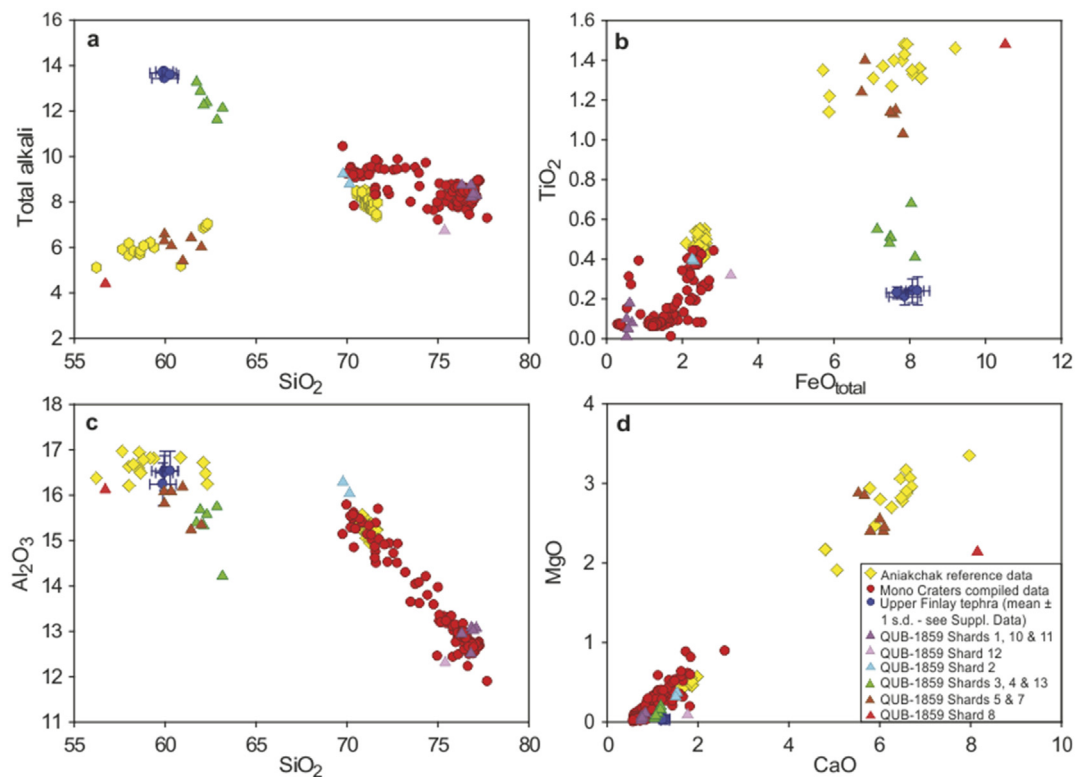
Extended Data Figure 3 | Timescale comparison. Age differences of the timescales NS1-2011 and GICC05 for the NEEM-2011-S1/NEEM ice cores (a) and WD2014 and WDC06A-7 for WDC (b). Differences before 86 CE (the age of the ice that is now at the bottom of the ice core NEEM-2011-S1) deriving from the annual-layer counting of the NEEM core are shown for major volcanic eruptions relative to the respective signals in NGRIP on the annual-layer counted GICC05 timescale. Marker events used for constraining the annual-layer dating (solid line) and for chronology evaluation (dashed lines) are indicated. Triangles mark volcanic signals. Also indicated is the difference between WD2014 and the Antarctic ice-core chronology (AICC2012)⁹², based on volcanic synchronization between the WDC and EDC96 ice cores.



Extended Data Figure 4 | Post-volcanic suppression of tree growth.

Superposed epoch analysis for large volcanic eruptions using the 28 largest volcanic eruptions (a); the 23 largest tropical eruptions (b); the five largest Northern Hemisphere eruptions (c); and eruptions larger than Tambora 1815 with respect to sulfate aerosol loading (d). Shown are growth anomalies of a

multi-centennial tree-ring composite record (N-Tree) 15 years after the year of volcanic sulfate deposition, relative to the average of five years before the events. Dashed lines indicate 95% confidence intervals (2 s.e.m.) of the tree-ring growth anomalies associated with the multiple eruptions.



Extended Data Figure 5 | Major-element composition for ice core tephra QUB-1859 and reference material. Shown are selected geochemistry data: SiO_2 versus total alkali ($\text{K}_2\text{O} + \text{Na}_2\text{O}$) (a); FeO (total iron oxides) versus TiO_2 (b); SiO_2 versus Al_2O_3 (c); and CaO versus MgO (d) from 11 shards extracted from the NEEM-2011-S1 ice core at 327.17–327.25 m depth, representing the age range 536.0–536.4 CE on the new, NS1-2011 timescale. Data for Late

Holocene tephra from Mono Craters (California) are from the compilation by ref. 90; data for Aniakhchak (Alaska) are from reference material published by ref. 88; and data for the early Holocene upper Finlay tephra, believed to be from the Edziza complex in the Upper Cordilleran Volcanic province (British Columbia), are from ref. 89. (See Supplementary Information for the Upper Finlay tephra.)

Extended Data Table 1 | Ice-core dating

Ice Core	Ice-core parameter	Dominant aerosol source	Deposition maximum
NEEM-2011-S1, (Greenland), 183-411m	Na, Cl nssS, nssS/Na nssCa, Mn, Ce BC, NH ₄ ⁺ , BC geometric mean particle size Sr, Mg, I, NO ₃ ⁻	sea salt marine biogenic emissions dust biomass burning various	winter summer spring summer
NEEM, (Greenland), 183-410m	<u>Na⁺</u> <u>Ca²⁺, particle count</u> <u>NH₄⁺, NO₃⁻</u> <u>conductivity, ECM, H₂O₂</u>	sea salt dust biomass burning various	winter spring summer
NEEM, (Greenland), 410-514m	Na, Sr, Cl, <u>Na⁺</u> nssS, nssS/Na nssCa, Mn, Mg, <u>particle count, Ca²⁺</u> BC, NH ₄ ⁺ , NO ₃ ⁻ , <u>NH₄⁺, NO₃⁻</u> conductivity, ECM, <u>H₂O₂</u>	sea salt marine biogenic emissions dust biomass burning various	winter summer spring summer
WDC, (Antarctica), 188-577m	Na, Sr nssS, nssS/Na, Br BC	sea salt marine biogenic emissions biomass burning	austral winter austral summer austral summer/fall

Year CE	Depth (m)	Event	Parameter	Independent age information
NEEM-2011-S1				
1258 [*]	183.49	volcano (tropical)	nssS	ice core (GICC05, Law Dome)
994 [†]	237.89	cosmic ray anomaly	¹⁰ Be	tree ring
946 [†]	247.21	volcano (NH, Tianshi)	nssS, tephra	historical observation
939 [†]	248.87	volcano (NH, Eldgjá)	nssS	historical observation
775 [*]	281.45	cosmic ray anomaly	¹⁰ Be	tree ring
626 [*]	310.01	volcano (NH)	nssS	historical observation
536 [*]	327.23	volcano (NH)	nssS, tephra	historical observation
WDC				
1258 [*]	188.91	volcano (tropical)	nssS	ice core (GICC05, Law Dome)
775 [*]	303.36	cosmic ray anomaly	¹⁰ Be	tree ring

Parameters used for annual-layer interpretation. Parameters measured by the CFA system in the field are underlined. NH, Northern Hemisphere.

*Stratigraphic age marker used to constrain annual-layer counting.

†Horizons used to evaluate the timescale.

Extended Data Table 2 | Annual-layer results using the StratiCounter program

Bipolar marker horizons								
Event [*]	Depth (m)			Annual layers between horizons [95% confidence interval]			Weighted average [2 σ]	Year [2 σ] [†] (BCE/CE)
	WDC	NEEM-2011-S1	NEEM	WDC	NEEM-2011-S1	NEEM		
Samalas	188.81	183.43	183.05					1259 [±2]
775 Event	303.37	281.25	280.89 [‡]	484 [481;487]	482 [479;485]	486 [483;490]	484 [±2]	775 [§]
UE 682	326.01	299.26	298.80	92 [91;93]	92 [91;93]	93 [93;95]	92 [±1]	683 [±1]
UE 574	351.67	320.33	319.95	108 [108;108]	109 [108;110]	109 [107;111]	108 [±1]	575 [±2]
UE 540	360.03	326.61	326.25	34 [34;35]	36 [35;37]	33 [33;34]	34 [±1]	541 [±2]
UE 266	423.81	377.43	377.15	274 [272;277]	273 [270;276]	272 [271;274]	273 [±2]	268 [±3]
UE -44	495.21		433.80	312 [310;315]		310 [309;313]	311 [±2]	-44 [±4]
UE -426			501.15			385 [383; 389]	385 [±4]	-429 [±6]

Greenland marker horizons							
Event	Depth (m)		Number annual layers [95% confidence]		Maximum likelihood year (wrt to 775 CE)		Independent Age (CE)
	NEEM-2011-S1	NEEM	NEEM-2011-S1	NEEM	NEEM-2011-S1	NEEM	
Samalas	183.43	183.05			1257	1261	1257/58 [*]
Eldgjá	248.76	248.40	317 [315;319]	320 [318;323]	940	941	939 [*]
775 Event	281.25	280.89 [‡]	165 [163;167]	166 [164;168]	775 [§]	775 [§]	775 [§]
UE 626/27	309.96	309.60	148 [147;149]	150 [148;152]	627	625	626/627 [*]
UE 536/37 ^{**}	327.20	326.84	92 [91;94]	89 [88;90]	535	536	536 [*]
UE 87/88 ^{††}	410.56	410.20	446 [443;449]	449 [446;452]	89	87	

Maximum-likelihood number of annual layers and confidence intervals derived from annual-layer counting between distinctive marker horizons and corresponding ages relative to the 775 CE ¹⁰Be event, wrt, with respect to.

*Unattributed events (UE) give volcanic signal and year of sulfate deposition based on final age models.

†Year calculated from the number of annual layers relative to the fixed age marker in 775 CE (negative numbers are years BCE).

‡Depth has been estimated from the average depth offset between NEEM-2011-S1 and NEEM.

§Fixed age marker based on the ¹⁰Be maximum annual value.

||Section with 6-m gap in the NEEM 2011-S1 core DRI data (this section is not used for calculating average age).

*This section is based on the NEEM field CFA data, since the DRI data does not cover the entire interval.

#Section is based on combined data set of DRI and field-measured CFA data. The number of annual layers in this section from manual interpretation by investigator 1 was 383 (±7), and that of investigator 2 was 393 (±8) layers. Most of the difference between the three layer counts occurred below 480 m (before 300 BCE), where data gaps were more frequent.

☆Independent age markers used to constrain annual-layer dating in a second iteration to derive the final ice-core age model NS1-2011.

**Tephra particles were extracted from the depth range 327.17–327.25 m (see Supplementary Data).

††Unattributed volcanic signal that was previously attributed to the historic 79 CE eruption of Vesuvius⁶⁴.

Extended Data Table 3 | Historical documentary evidence for key volcanic eruption age markers 536-939 CE

Year (Start)	Summary	Translation	Selected source(s)	Confidence
536	Diminished sunlight for >12 months (Mediterranean)	For the sun gave forth its light without brightness, like the moon, during this whole year, and it seemed exceedingly like the sun in eclipse, for the beams it shed were not clear nor such as it is accustomed to shed.	Procopius, History of the Wars, H.B. Dewing, trans. (Harvard, 1916), 4.14. (five additional sources)	High; Eyewitness or contemporary with a reliable chronology.
626	Diminished sunlight for 9 months (Mediterranean, NW Europe)	There was an eclipse of the sun and it lasted from October [626] until June [627], that is, for nine months. Half of its disc was eclipsed and the other half not; only a little of its light was visible.	Theophilus of Edessa's Chronicle, R.G. Hoyland, trans. (Liverpool, 2011), p. 73. (five additional sources)	High; Eyewitness or contemporary but with some chronological uncertainty.
939	Diminished sunlight (Mediterranean, NW Europe)	We observed the sun: it did not have any strength, brightness, nor heat. Indeed, we saw the sky and its colour changed, as if flushed. And others said that the sun was seen as if halved.	Annales Casinates, Monumenta Germaniae Historica, Scriptores, ed. G.H. Pertz (Hannover, 1839), p. 172. Trans. for this paper by C. Kostick. (three additional sources)	High; Eyewitness or contemporary with a reliable chronology.

A comprehensive list of sources, including translations and assessment of the confidence placed in each source and its chronological information is given in Supplementary Data. NW, northwest.

Extended Data Table 4 | Large volcanic eruptions during the past 2,500 years

Rank	Year	Volc. SO ₄ ²⁻ Greenland (kg km ⁻²)	Volc. SO ₄ ²⁻ Antarctica (kg km ⁻²)	Global forcing* (W m ⁻²)	Cold year	N-Tree (z scores; 1000-99)	T _{Europe/Arctic} (°C; 1961-90)	Volcanot/ Region
1	-426	99.8	78.2	-35.6	-425	-2.74		UE -426
2	1258	90.4	73.4	-32.8	1258	-1.43	-0.91	Samalas/Indonesia
3	-44	100.6	15.4	-23.2	-43	-3.33		Chiltepe?/Nicaragua
4	1458	39.0	63.6	-20.5	1459	-2.31	-1.03	Kuwaae/Vanuatu
5	540	61.2	34.4	-19.1	541	-2.57	-1.48	Ilopango?/El Salvador
6	1815	39.7	45.8	-17.1	1816	-2.51	-1.55	Tambora/Indonesia
7	1230	56.4	23.1	-15.9	1230	-1.71	-0.65	UE 1230
8	1783	135.8		-15.5	1783	-1.16	-0.97	Laki/Iceland
9	682	38.4	38.7	-15.4	682	-0.95	-0.96	Pago?/New Britain
10	574	38.3	34.1	-14.5	574	-2.46	-0.94	Rabaul?/New Britain
11	266	61.0	11.3	-14.5	268	-1.70	-0.72	UE 266
12	1809	34.6	25.4	-12.0	1810	-2.18	-1.23	UE 1809
13	1108	48.3	11.6	-12.0	1109	-1.99	-1.15	UE 1108
14	1641	44.2	14.9	-11.8	1641	-2.31	-1.19	Parker/Philippines
15	1601	39.2	18.7	-11.6	1601	-2.62	-1.50	Huaynaputina/Peru
16	169	39.1	18.4	-11.5	170	-0.80	-0.94	UE 169
17	1171	37.0	19.5	-11.3	1171	-0.91	-0.88	UE 1171
18	536	99.0		-11.3	536	-3.36	-1.74	UE 536
19	1695	28.6	22.5	-10.2	1696	-1.63	-1.28	UE 1695
20	939	88.7		-10.1	940	-1.81	-1.44	Eldgjá/Iceland
21	1286	27.6	20.8	-9.7	1288	-1.49	-0.65	Quilotoa?/Ecuador
22	433	20.6	27.2	-9.6	432	-0.45	-0.25	UE 433
23	87	83.1		-9.5	87	-0.22	-0.49	UE 87
24	1345	27.9	19.1	-9.4	1346	-2.18	-1.48	El Chichon?/Mexico
25	626	72.2		-8.2	627	-3.00	-0.93	UE 626

Years with negative numbers are BCE. Tentative attribution of ice-core signals to historic volcanic eruptions is based on the Global Volcanism Program volcanic eruption database⁸³. Average (summer) temperature for the associated cold year is given for the average of Europe and the Arctic³. Volc., volcanic.

*Total global aerosol forcing was estimated by scaling the total sulfate flux from both polar ice sheets to the reconstructed total (that is, time integrated) aerosol forcing for Tambora 1815⁷ (Methods); for high-latitude Northern Hemisphere eruptions, Greenland fluxes were scaled by a factor of 0.57⁶.

†Unattributed volcanic events (UE) and tentative attributions for non-documented historic eruptions (?) are marked.

Extended Data Table 5 | Post-volcanic cooling

Rank	Year	JJA temperature anomaly (°C)	Volcanic event(s)	Decade	JJA temperature anomaly (°C)	Volcanic event(s)
1	1821	-1.82	1815 , 1821	1600-1609	-1.17	<u>1595</u> , 1601
2	1601	-1.82	1600	536-545	-1.12	536 , 540
3	1675	-1.78	<u>1673</u>	1812-1821	-1.10	1809 , 1815
4	536	-1.67	536	1453-1462	-1.01	1453 , 1458
5	800	-1.66	800	1587-1596	-0.98	<u>1585</u> , 1590, 1595
6	1816	-1.64	1815	1107-1116	-0.96	1108 , 1115
7	1453	-1.57	1453	1344-1353	-0.87	1341, 1345
8	1633	-1.56		351-360	-0.83	351, 358, 360
9	1109	-1.56	1108	1692-1701	-0.82	<u>1693</u> , 1695
10	1608	-1.53		413-422	-0.79	411, 418
11	544	-1.50	540	1463-1472	-0.79	1458 , 1463, 1470
12	574	-1.48	574	1127-1136	-0.79	<u>1127</u>
13	1695	-1.47	1693, 1695	389-398	-0.78	<u>388</u> , 393
14	543	-1.46	540	1672-1681	-0.77	<u>1673</u>
15	541	-1.43	540	1632-1641	-0.76	1637, 1641
16	549	-1.43	547	1258-1267	-0.76	1258

Rank	Year	Tree growth anomaly (z-scores)	Volcanic event(s)	Decade	Tree growth anomaly (z-scores)	Volcanic event(s)
1	536 [*]	-3.4	536	536-545	-2.2	536 , 540
2	-43 [*]	-3.3	-44	1812-1821	-2.2	1809 , 1815
3	627 [*]	-3.0	626	1453-1462	-2.0	1453 , 1458
4	543	-3.0	540	-43 to -34	-2.0	-46, -44
5	-360	-2.9	<u>-360</u>	1601-1610	-2.0	1600
6	-35	-2.8	-35	-361 to -352	-1.8	<u>-360</u> , <u>-356</u>
7	-425 [*]	-2.7	-426	1463-1472	-1.7	1458 , 1463
8	-42 [*]	-2.7	-44	1832-1841	-1.7	1831 , 1835
9	546	-2.6	540	1341-1350	-1.7	1344
10	-140 [*]	-2.6	-141	546-555	-1.6	540 , 547
11	541	-2.6	540	1673-1682	-1.5	<u>1673</u>
12	544	-2.6	540	-427 to -418	-1.5	-426
13	545	-2.5	540	1330-1339	-1.4	1329, 1336
14	574 [*]	-2.5	574	1638-1647	-1.4	1641 , 1646
15	-354 [*]	-2.5	<u>-356</u>	1699-1708	-1.4	1695 , 1708
16	-38	-2.5		1285-1294	-1.4	1286

Coldest years and decades (1–2000 CE, JJA temperature with respect to 1901–2000) for Europe³ and years (500 BCE–1250 CE) and decades (500 BCE–2000 CE) with strong growth reduction in the N-Tree composite (with respect to 1000–1099). Ages of the volcanic events from the ice cores reflect the start of volcanic sulfate deposition in Greenland (NS1-2011 timescale) with the largest 40 events indicated in bold letters and tropical eruptions underlined. Years with negative numbers are before the Common Era (BCE).

*Latewood frost ring in bristlecone pines within one year²⁴.